



Title	Development of Electrochromic Transistors using Amorphous Tungsten Oxide Thin Film as the Active Layer
Author(s)	小野里, 尚記
Citation	北海道大学. 博士(工学) 甲第14130号
Issue Date	2020-03-25
DOI	10.14943/doctoral.k14130
Doc URL	http://hdl.handle.net/2115/78543
Type	theses (doctoral)
File Information	Takaki_Onozato.pdf



[Instructions for use](#)

**Development of Electrochromic Transistors
using Amorphous Tungsten Oxide Thin Film
as the Active layer**

TAKAKI ONOZATO

**Graduate School of Information Science and Technology
Hokkaido University**

Content

1. General Introduction.....1

1.1 Background and Introduction of Present study 1

1.2 Electrochromic devices..... 3

1.2.1 Tungsten trioxide (WO₃) as an active material..... 4

1.2.2 Solid electrolyte..... 4

1.2.3 NiO thin film as the counter layer 7

1.3 Recent practical electrochromic devices..... 8

1.4 Previous Study 9

1.5 Research strategy and Outline of thesis 10

References..... 14

2. Experimental Method25

2.1 Pulsed Laser Deposition (PLD) method 25

2.2 Structural characterization 28

2.2.1 XRD measurement 28

2.2.2 Scanning transmission electron microscopy (STEM) 29

2.2.3 Optical property measurement..... 30

2.3 Operating mechanism 30

References..... 32

3. A transparent electrochromic metal-insulator switching device with three-terminal transistor geometry36

3.1 Introduction..... 36

3.2 Experimental..... 39

3.3 Result 41

Content

3.4 Discussion.....	45
3.5 Conclusion	47
References.....	49
4. Fast operation of a WO₃-based solid-state electrochromic transistor	59
4.1 Introduction.....	59
4.2 Experimental.....	61
4.3 Result and discussion.....	62
4.4 Conclusion	63
References.....	64
5. An oxide-based flexible electrochromic transistor under mechanical stress.....	73
5.1 Introduction.....	73
5.2 Experimental.....	75
5.3 Result	76
5.4 Discussion.....	79
5.5 Conclusion	81
References.....	83
6. Summary	90
Acknowledgments.....	96
Publication list	98
Presentation list.....	101
Award list.....	106

1. General Introduction

1.1. Background and Introduction of Present study

Recent years have witnessed a growing interest in transition metal oxides (TMOs) as an important component for the development of innovative devices due to their versatile physical properties such as electrical conductivity, optical, and magnetic properties¹⁻⁴. The variation of the intriguing functional properties in TMOs originates from the flexibility of multi-valence states in the transition-metal (TM) cations, which depend on the stoichiometry and their nearest neighboring ions. For this reason, TM ions often forms various phases with drastic differences in the electronic structure, and such behavior makes them attractive as the ideal platform for the development of advanced electronic devices. One of the effective methods for modulating their property is the use of redox reaction of TMOs since the valence states of TM ions can be controlled with the oxygen-anion ratio, hydrogen impurities, and their coordination numbers^{5,6}. Thus, the control of oxygen proficiency/deficiency and protonation of TMOs are the most promising way for demonstrating devices with multifunctional switching abilities.

Conventional method for triggering the redox reaction has been the use of electrolysis with liquid electrolyte, which can induce oxidation, oxygen-vacancy formation, and protonation of TMOs by applying an electric field at room temperature (RT). In this method, the ionic dopants can penetrate into the bulk region of TMOs and can change their properties. In addition, after the removal of an applied electric field, the ionic dopants remain in the TMOs, and the application of a reverse electric field can remove

1. General Introduction

them. Therefore, electrochemical modification can be utilized for switching TMO-based devices in a non-volatile way. This method has the advantage of being a room temperature operation since the conventional approach for controlling the amount of oxygen ions /proton in TMOs is heating under an oxidative/reductive atmosphere⁷⁻¹⁰. However, the electrochemical approach has not been applied to practical devices because it can suffer from the risk of liquid-leakage.

Water-infiltrated nanoporous glass is a good candidate for liquid-leakage-free electrolyte, where the liquid water is confined in the nanopores in glass, and no leakage of the liquid water can occur because of the large surface tension between the water and glass. Furthermore, water contains hydroxide (OH^-) and hydrogen (H^+), which are strong oxidizing agent (OH^-) and reducing agent (H^+) for TMOs, and their electro-optical and electromagnetic properties can be reversibly controlled by applying a positive/negative electric field¹¹⁻¹⁴.

This dissertation focuses on metal oxides because transition metal oxides (TMOs) change their optical property or magnetic property together with the electrical property in a redox reaction using water (Figure 1)¹⁵⁻¹⁷. Tungsten trioxide (WO_3) was chosen as the active TMO^{18, 19} since WO_3 shows an electrochromic phenomenon in which optical and electrical properties simultaneously change by a redox reaction. Therefore, it can be used in electrochromic transistors (ECTs), which have attracted increasing attention as advanced multifunctional devices utilizing electrochromism and switching of electron transport in a nonvolatile manner. For example, a dual way of storing/reading of information becomes possible with optical and electrical signals if they are combined

with display technology. Thus, ECTs are appropriate for advanced multifunctional switching devices.

1.2. Electrochromic devices

The electrochromism is defined as a phenomenon in which a material undergoes a reversible optical color change when an electrical current is applied to it. During the electrochromic phenomenon, the external stimulus is an electrical. Similarly, thermochromism reversibly changes the optical properties due to thermal stimulus, and the external stimulus of photochromism is light. Electrochromism has been known for a long time ²⁰. In 1704, Diesbach *et al.* discovered hexacyan-iron, which changes from transparent to blue. Tungsten trioxide (WO_3) ^{18, 21, 22} is the most famous electrochromic material among commonly used electrochromic materials ²³⁻³³. Electrochromism in bulk WO_3 was reported in the 1930s by Kobosew and Nekrassow. In 1969, S.K. Deb *et al* demonstrated the electrochromism in the WO_3 thin film ^{21, 34}, but the mechanism of its operation was clarified later in 1975 by B.W. Faughnan *et al.* It was reported that electrochromism in WO_3 occurs by ionic-reaction ³⁵.

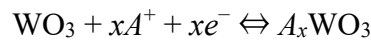
The structure of a typical electrochromic device shown in **Figure 2**, which consists of the following parts:

- (1) Transparent electrode to assist electron transfer.
- (2) An electrochromic active layer made of an electrochromic material that causes optical changes.

- (3) Electrolyte layer that supplies ions that contribute to the electrochemical reaction.
- (4) Counter electrode layer that performs a redox reaction opposite to that of the electrochromic active layer.

1.2.1. Tungsten trioxide (WO₃) as an active material

WO₃ is a colorless transparent insulator with a bandgap of 2.6-3.0 eV ³⁶. When Alkali-ion or proton is electrochemically inserted to WO₃, it changes to a blue metal $A_x\text{WO}_3$ called Tungsten bronze ³⁷.



Initially, the valence state of tungsten in tungsten trioxide (WO₃) is a stable W⁶⁺. When a proton (H⁺) is inserted, to maintain the charge balance, hexavalent tungsten becomes W⁵⁺. Thus, this process is a carrier-doping, and $A_x\text{WO}_3$ becomes metalized. When a mixed-valence state of W⁵⁺ and W⁶⁺ is created, localized electrons in W⁵⁺ can absorb light and transfer to the W⁶⁺ site, which changes the color ^{35,38}. The electron in the 5*d* orbital of W can also go through a *d-d* transition in the *d* orbital, which can also absorb light ³⁹. The carrier doping also enables plasma absorption.

1.2.2. Solid electrolyte

An electrolyte is required to supply protons to the active WO₃ layer. Although many organic and inorganic electrolytes have been reported ⁴⁰⁻⁵², the conventional EC device usually has a risk of liquid leakage because it uses liquid electrolyte. Therefore, solid

1. General Introduction

electrolyte was implemented in this research, and C12A7 with nanopores or TaO_x was selected as the solid electrolyte.

Water-infiltrated nanoporous 12CaO·7Al₂O₃ glass (calcium aluminate with nanopores, CAN)

One of the two solid electrolytes used in this research is a porous thin film made of 12CaO·7Al₂O₃ (C12A7), an alumina cement material, fabricated at room temperature under high oxygen pressure. Inside the thin film, nanopores with a diameter of ~10 nm are present at high density. In 2009, Prof. Hiromichi Ohta (currently Professor of Research Institute for Electronic Science, Hokkaido University) developed a method to easily produce porous membranes, which was named “Calcium Aluminate with Nanopore” (CAN) ^{53, 54}. Due to the capillary action, all nanopores inside the CAN thin film exhibit moisture from the atmosphere. This CAN thin film can be used as a solid electrolyte without leakage like a wet sponge. Furthermore, by applying a voltage in a CAN film sandwiched between two electrodes, H⁺ and OH⁻ present in the nanopore can be used as a strong reducing/oxidizing agent or strong dielectric ^{15, 54, 55}.

There are two ways of using CAN thin films for the modulation of electrochromic devices. As described above, by applying a voltage to the CAN thin film, it is possible to move protons H⁺ and hydroxide ions OH⁻ in the film to the both ends of the CAN thin film. The reaction depends on the bandgap of the active layer material, as shown in **Figure 3**. When the conduction band minimum (CBM) of the active layer material in contact with the CAN is higher than the hydrogen level (*eg* SrTiO₃, KTaO₃), H⁺ attracted to the

1. General Introduction

active layer does not react with the active layer and forms a double-layered electric capacitor, which can accumulate high-density charge carriers on the active layer electrode surface ⁵⁵. On the other hand, when the CBM of the active layer material is lower than the hydrogen level, proton H^+ enters the active layer and causes an electrochemical reaction ^{15,56}. In this study, CBM of active WO_3 is lower than the hydrogen level, and an electrochemical reaction can be expected when proton H^+ entered the active layer.

Tantalum oxide (TaO_x)

To enhance the device performance, an excellent ionic conductor is required as the electrolyte layer (gate insulator) ⁵⁷⁻⁵⁹. Therefore, Tantalum oxide (TaO_x) film was implemented as the solid electrolyte due to its high ionic conductivity. **Figure 4** shows a Cole-Cole plot of the TaO_x and CAN film measured at RT in air. In both TaO_x and CAN, a semicircle was observed on the high-frequency side. The semicircle of TaO_x ends around 1 kHz. This relationship is similar to that of CAN, which indicates that water molecules are present in the TaO_x film. However, the ionic conductivity of TaO_x (125 nS cm^{-1}) is 5 times higher than that of CAN (24 nS cm^{-1}). The difference in the ionic conductivity is not surprising since the CAN film has a nano-porous structure while TaO_x film has a nano-pillar array structure. Furthermore, it is likely that the water contained in TaO_x film is not perfectly pure and slightly acidic due to the dissolution of organic compounds like carbon dioxide.

1.2.3. NiO thin film as the counter Layer

A typical electrochromic device requires a counter electrode layer that performs a redox reaction opposite to that in the electrochromic active layer. In this study, proton H^+ in the solid electrolyte layer thin film is injected into the electrochromic active amorphous WO_3 (a- WO_3) layer and reacts ($WO_3 + H^+ + xe^- \Leftrightarrow H_xWO_3$). In addition to protons, the electrolysis of water produces OH^- ions as well, so a counter layer that absorbs OH^- is necessary. In this study, NiO was used as the counter layer (OH^- ion absorber). NiO is known as an oxidative electrochromic material that reacts with OH^- ions to become NiOOH, and the color changes from colorless to brown. The reaction mechanism from colorless and transparent NiO to brown NiOOH occurs as follows ^{60,61}:



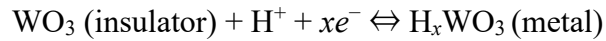
It is an oxidative coloring reaction in which divalent Ni^{2+} forms the decolored state and trivalent Ni^{3+} forms the colored state. The counter layer NiO also serves as a buffer material for the solid-electrolyte and the top gate electrode. For example, when ITO electrode was deposited on the solid-electrolyte layer directly, the resistance of ITO increased rapidly with time and lost its role as an electrode. The phenomenon is related to the fact that ITO does not have a sufficient reaction mechanism with the OH^- ion from the electrolyte. In other words, since NiO can act as a counter electrode as well as a buffer layer between the electrode and the solid electrolyte layer CAN thin film, the NiO layer was expected to enable reversible electrochemical reactions in the device.

1.3. Recent practical electrochromic device

There are various types of electrochromic devices, which are categorized in **Figure 5**. The electrochromic material can be classified as liquid or a solid type. When the electrochromic material is liquid type, the electrolyte material and the counter material should be in a liquid state. If the electrochromic material is solid type, there are three types of electrolyte layers: solid, gel, and liquid type. In case of liquid type, there are two types of counter layer, a liquid type, and a solid type. On the other hand, for solid type electrolyte layer, the counter layer is also solid type. Examples of solid-type counter layers include thin-film types fabricated by the vacuum process and thick-film (bulk) types formed by conventional coating methods. The most famous electrochromic window is used in the Boeing 787 aircraft (**Figure 6**), which has a gel-electrolyte type electrochromic device. However, when the electrolyte layer is liquid or gel type, there is a risk of electrolyte leakage. In fact, in an electrochromic antiglare mirror, an accident of electrolyte leakage has been reported when the mirror broke. To completely prevent leakage, sealing of the electrolyte is necessary, which is not economically viable. This issue can potentially be resolved by utilizing solid electrolyte since it removes the source of leakage.

In addition, although WO_3 is used as an active material for many electrochromic devices, they cannot make full use of the electrical characteristics of WO_3 . As described above, WO_3 has a colorless and transparent insulator but become a blue metal if Alkali ion or Proton is introduced.

1. General Introduction



However, conventional electrochromic devices have a parallel plate structure (electrochromic display), and the insulator to a metal transition cannot be used. This limitation was overcome with a new electrochromic device using a three-terminal transistor structure ^{15, 56}, but practical usages are difficult because liquid-electrolytic was implemented.

1.4. Previous Study

Recently, many researchers reported a thin film transistor (TFT)-type electrochromic (EC) device using WO_3 as the active material ⁶²⁻⁶⁸. P. Barquinha *et al.* and X. Meng *et al.* reported a TFT-type EC device with WO_3 thin film deposited at low temperature as the active layer ^{62, 67}. Although they succeeded in utilizing the change in channel conductivity in addition to the color change, they used a liquid-electrolyte or ionic liquid as an electrolyte layer (gate insulator). To avoid potential leakage, Prof. Hiromichi Ohta's research group used CAN thin film (Calcium Aluminate with Nanopore) as a gate insulator on WO_3 thin film heteroepitaxial grown on sapphire substrate and fabricated an all-solid-state TFT structure. The simultaneous modulation of the color tone and conductivity was successful, but the use of single-crystal sapphire substrate (~ 4000 JPY) and the high temperature growth of epitaxial WO_3 greatly increase the cost. To make the

1. General Introduction

device economically viable, this research focused on developing amorphous WO_3 electrochromic transistor on glass substrate instead of an expensive single crystal substrate using a room temperature process.

1.5. Research strategy and Outline of thesis

Utilizing the changes in both the optical and electrical properties of WO_3 enables multifunctional electronic devices such as information display/storage device having a memory function. However, past researches on electrochromic devices mostly focused on electrochromic display configuration (parallel plate), which does not make use of the change in the electrical conductivity of the active layer. To fully utilize the functional properties of WO_3 , it is necessary to use a three-terminal structure such as a TFT, and solid electrolyte is preferred for preventing the leakage of liquid electrolyte. **Figure 7** shows the concept image of an all-solid electrochromic transistor, which is based on the protonation/deprotonation of WO_3 . This approach is promising for the realization of simultaneous electrical switching between colorless/colored and insulating/conducting states ¹⁷. However, practical aspects like performance enhancements and cost reduction have not been addressed.

The aim of this research is developing high-performance all-solid-state three terminal electrochromic WO_3 transistor at a commercially viable cost. To ease the device fabrication, a room temperature process was investigated, and a TFT-type device was prepared on glass substrates to reduce the raw materials cost. Amorphous WO_3 film was

1. General Introduction

used as an active layer, and a solid electrolyte was formed on the thin film as a gate insulator. ITO thin film was used as a source-drain electrode for transparency, and a NiO / ITO bilayer film was used as a gate electrode to enable reversibility. Lastly, to meet the high demand for mechanical flexibility in electronic devices, the development of flexible high-speed electrochromic transistors was also attempted.

This dissertation is mainly composed of three sections.

1. A transparent electrochromic transistor with three-terminal geometry ¹⁷

Proton and hydroxide play an essential role for tuning the functionality of oxides due to their ability to control the oxygen stoichiometry and electronic state. Tungsten trioxide (WO_3), a well-known electrochromic (EC) material, was chosen as the active layer. To utilize both the electrochromism and metal-insulator (MI) transition, conventional parallel-plate configuration was changed to three-terminal transistor configuration. This section demonstrates the fabrication and operation of a transparent switchable EC-MI device with three-terminal TFT-type structure using amorphous a-WO_3 channel layer, which was fabricated on glass substrate at room temperature. Water-infiltrated nanoporous glass, CAN (calcium aluminate with nano-pores), was used as a liquid-leakage-free solid gate insulator. Initially, the as-prepared device was fully transparent in the visible region. Upon the application of positive gate voltage, the active channel became dark blue, and electrical resistivity of the a-WO_3 layer drastically decreased due to protonation. Upon the application of negative gate voltage, the active channel

1. General Introduction

deprotonated and returned to a transparent insulator. Excellent cyclability was observed, and the transparent EC-MI switching device demonstrated in this section provides a pioneering route for the development of advanced smart windows.

2. Fast operation of a WO_3 -based solid-state electrochromic transistor⁶⁹

The abovementioned electrochromic transistors (ECTs) attract attention as advanced memory technology because one can use both electrochromism and switching of electrical conductivity in a nonvolatile manner. However, the operating speed is slow (operating time >1 min) compared to liquid-based ECTs (~ 20 s) due to their asymmetric gate-source electrode configuration. In this section, a fast operation of a solid-state ECT with three terminal gate-source-drain electrodes was demonstrated using an amorphous WO_3 film as the electrochromic material and amorphous TaO_x as the solid electrolyte. By the insertion of a thin ZnO layer between the source and drain electrodes to achieve pseudo symmetric gate-source electrode configuration, the operation time was greatly reduced to less than 1 s at ± 3 V application while keeping the on-to-off ratio of ~ 30 . The present approach is effective to improve the operating speed of ECTs and may be practically used in advanced memory technologies.

3. An oxide-based flexible electrochromic transistor under mechanical stress⁷⁰

Today mechanical flexibility has become an important feature for electronic devices, especially in flat display panels. Here, the device operation of a tungsten oxide based flexible electrochromic transistor (ECT) was demonstrated. The device was fabricated on

1. General Introduction

0.1-mm-thick polyethylene terephthalate film and can be operated by applying voltage of ± 3 V for 1 s when the radius of curvature was larger than 16 mm, indicating that the flexible ECT exhibited a strong resistance to static strains. However, the resistance of the channel increased by fatigues from applying cyclic flexural strains. Present flexible ECT would highly be useful for the economically viable curved display panels. However, its vulnerability to fatigue needs improvements for other applications.

References

- [1] J. Mannhart and D. G. Schlom, *Nature* **430**, 620-621 (2004).
- [2] H. Takagi and H. Y. Hwang, *Science* **327**, 1601-1602 (2010).
- [3] E. Dagotto, *Science* **309**, 257-262 (2005).
- [4] T. Onozato, T. Katase, A. Yamamoto, S. Katayama, K. Matsushima, N. Itagaki, H. Yoshida and H. Ohta, *J. Phys.: Condens. Matter* **28**, 255001 (2016).
- [5] M. A. Hayward and M. J. Rosseinsky, *Chem. Mater.* **12**, 2182-2195 (2000).
- [6] J. B. Goodenough, *Rep. Prog. Phys.* **67**, 1915 (2004).
- [7] Z. Shao and S. M. Haile, *Nature* **431**, 170-173 (2004).
- [8] A. M. Chippindale, P. G. Dickens and A. V. Powell, *J. Solid State Chem.* **93**, 526-533 (1991).
- [9] V. N. Andreev, V. M. Kapralova and V. A. Klimov, *Physics of the Solid State* **49**, 2318-2322 (2007).
- [10] H. Jeen, W. S. Choi, M. D. Biegalski, C. M. Folkman, I. C. Tung, D. D. Fong, J. W. Freeland, D. Shin, H. Ohta, M. F. Chisholm and H. N. Lee, *Nature Materials* **12**, 1057-1063 (2013).
- [11] H. Ji, J. Wei and D. Natelson, *Nano Lett.* **12**, 2988-2992 (2012).
- [12] J. Jeong, N. Aetukuri, T. Graf, T. D. Schladt, M. G. Samant and S. S. P. Parkin, *Science* **339**, 1402-1405 (2013).
- [13] O. T. Tambunan, M. Y. Lee, D. H. Kim, K. J. Parwanta and C. U. Jung, *Journal of the Korean Physical Society* **64**, 1845-1848 (2014).
- [14] N. Lu, P. Zhang, Q. Zhang, R. Qiao, Q. He, H.-B. Li, Y. Wang, J. Guo, D. Zhang, Z. Duan, Z. Li, M. Wang, S. Yang, M. Yan, E. Arenholz, S. Zhou, W. Yang, L. Gu, C.-W. Nan, J. Wu, Y. Tokura and P. Yu, *Nature* **546**, 124-128 (2017).
- [15] T. Katase, K. Endo, T. Tohei, Y. Ikuhara and H. Ohta, *Adv. Electron. Mater.* **1**, 1500063 (2015).
- [16] T. Katase, Y. Suzuki and H. Ohta, *Adv. Electron. Mater.* **2**, 1600044 (2016).
- [17] T. Katase, T. Onozato, M. Hirono, T. Mizuno and H. Ohta, *Sci. Rep.* **6**, 25819 (2016).
- [18] C. G. Granqvist, *Sol. Energy Mater. Sol. Cells* **60**, 201-262 (2000).
- [19] P. P. Gonzalez-Borrero, F. Sato, A. N. Medina, M. L. Baesso, A. C. Bento, G. Baldissera, C. Persson, G. A. Niklasson, C. G. Granqvist and A. F. da Silva, *Appl. Phys.*

I. General Introduction

Lett. **96**, 3 (2010).

[20] J. R. Platt, *The Journal of Chemical Physics* **34**, 862-863 (1961).

[21] S. K. Deb, *The Philosophical Magazine: A Journal of Theoretical Experimental and Applied Physics* **27**, 801-822 (1973).

[22] C. G. Granqvist, *Sol. Energy Mater. Sol. Cells* **92**, 203-208 (2008).

[23] K. Itaya, K. Shibayama, H. Akahoshi and S. Toshima, *J. Appl. Phys.* **53**, 804-805 (1982).

[24] R. J. Colton, A. M. Guzman and J. W. Rabalais, *J. Appl. Phys.* **49**, 409-416 (1978).

[25] L. D. Burke and O. J. Murphy, *J. Electroanal. Chem.* **112**, 379-382 (1980).

[26] D. Tench and L. F. Warren, *J. Electrochem. Soc.* **130**, 869-872 (1983).

[27] I. Shimizu, M. Shizukuishi and E. Inoue, *J. Appl. Phys.* **50**, 4027-4032 (1979).

[28] S. Gottesfeld, *J. Electrochem. Soc.* **127**, 272-277 (1980).

[29] F. B. Kaufman, A. H. Schroeder, E. M. Engler and V. V. Patel, *Appl. Phys. Lett.* **36**, 422-425 (1980).

[30] K. Kaneto, K. Yoshino and Y. Inuishi, *Jpn. J. Appl. Phys.* **22**, L412-L414 (1983).

[31] T. Kobayashi, H. Yoneyama and H. Tamura, *J. Electroanal. Chem.* **177**, 293-297 (1984).

[32] J. Livage and J. Lemerle, *Annu. Rev. Mater. Sci.* **12**, 103-122 (1982).

[33] H. Yamamoto, T. Sugiyama and M. Tanaka, *Jpn. J. Appl. Phys. Part 2 - Lett.* **24**, L305-L307 (1985).

[34] S. K. Deb, *Appl. Opt.* **8 Suppl 1**, 192-195 (1969).

[35] B. W. Faughnan, R. S. Crandall and M. A. Lampert, *Appl. Phys. Lett.* **27**, 275-277 (1975).

[36] P. P. González-Borrero, F. Sato, A. N. Medina, M. L. Baesso, A. C. Bento, G. Baldissera, C. Persson, G. A. Niklasson, C. G. Granqvist and A. F. d. Silva, *Appl. Phys. Lett.* **96**, 061909 (2010).

[37] J. Vondrák and J. Bludská, *Solid State Ionics* **68**, 317-323 (1994).

[38] S. K. Deb, *Sol. Energy Mater. Sol. Cells* **92**, 245-258 (2008).

[39] S. K. Deb, *Sol. Energy Mater. Sol. Cells* **25**, 327-338 (1992).

[40] M. Green and D. Richman, *Thin Solid Films* **24**, S45-S46 (1974).

[41] M. Green and K. S. Kang, *Thin Solid Films* **40**, L19-L21 (1977).

[42] G. G. Barna, *J. Electron. Mater.* **8**, 153-173 (1979).

[43] M. Miyamura, S. Tomura, A. Imai and S. Inomata, *Solid State Ionics* **3-4**, 149-152

(1981).

[44] S. K. Mohapatra, G. D. Boyd, F. G. Storz, S. Wagner and F. Wudl, *J. Electrochem. Soc.* **126**, 805-808 (1979).

[45] A. T. Howe, S. H. Sheffield, P. E. Childs and M. G. Shilton, *Thin Solid Films* **67**, 365-370 (1980).

[46] J. P. Randin and R. Viennet, *J. Electrochem. Soc.* **129**, 2349-2354 (1982).

[47] W. C. Dautremont - Smith, G. Beni, L. M. Schiavone and J. L. Shay, *Appl. Phys. Lett.* **35**, 565-567 (1979).

[48] L. M. Schiavone, W. C. Dautremont - Smith, G. Beni and J. L. Shay, *Appl. Phys. Lett.* **35**, 823-825 (1979).

[49] M. Shizukuishi, E. Kaga, I. Shimizu, H. Kokado and E. Inoue, *Jpn. J. Appl. Phys.* **20**, 581-586 (1981).

[50] H. J. Stocker, S. Singh, L. G. VanUitert and G. J. Zydzik, *J. Appl. Phys.* **50**, 2993-2994 (1979).

[51] T. Saito, Y. Ushio, M. Yamada and T. Niwa, *Solid State Ionics* **40-41**, 499-501 (1990).

[52] M. J. Duggan, T. Saito and T. Niwa, *Solid State Ionics* **62**, 15-20 (1993).

[53] H. Ohta, *Journal of Materials Science* **48**, 2797-2805 (2013).

[54] H. Ohta, Y. Sato, T. Kato, S. Kim, K. Nomura, Y. Ikuhara and H. Hosono, *Nat. Commun.* **1**, 118 (2010).

[55] H. Ohta, T. Mizuno, S. Zheng, T. Kato, Y. Ikuhara, K. Abe, H. Kumomi, K. Nomura and H. Hosono, *Adv. Mater.* **24**, 740-744 (2012).

[56] T. Katase, K. Endo and H. Ohta, *Physical Review B* **90**, 161105 (2014).

[57] M. J. Duggan, T. Saito and T. Niwa, *Solid State Ionics* **62**, 15-20 (1993).

[58] K. Tajima, Y. Yamada, S. Bao, M. Okada and K. Yoshimura, *Solid State Ionics* **180**, 654-658 (2009).

[59] M. Zhu, Z. Zhang and W. Miao, *Appl. Phys. Lett.* **89** (2006).

[60] I. C. Faria, R. Torresi and A. Gorenstein, *Electrochim. Acta* **38**, 2765-2771 (1993).

[61] X. H. Xia, J. P. Tu, J. Zhang, X. L. Wang, W. K. Zhang and H. Huang, *Sol. Energy Mater. Sol. Cells* **92**, 628-633 (2008).

[62] P. Barquinha, S. Pereira, L. Pereira, P. Wojcik, P. Grey, R. Martins and E. Fortunato, *Adv. Electron. Mater.* **1** (2015).

[63] M. Wang, S. Shen, J. Ni, N. Lu, Z. Li, H. B. Li, S. Yang, T. Chen, J. Guo, Y. Wang, H. Xiang and P. Yu, *Adv. Mater.* **29** (2017).

I. General Introduction

- [64] S. G. Altendorf, J. Jeong, D. Passarello, N. B. Aetukuri, M. G. Samant and S. S. Parkin, *Adv. Mater.* **28**, 5284-5292 (2016).
- [65] X. Leng, J. Pereiro, J. Strle, G. Dubuis, A. T. Bollinger, A. Gozar, J. Wu, N. Litombe, C. Panagopoulos, D. Pavuna and I. Bozovic, *npj Quantum Mater* **2** (2017).
- [66] C. ViolBarbosa, J. Karel, J. Kiss, O. D. Gordan, S. G. Altendorf, Y. Utsumi, M. G. Samant, Y. H. Wu, K. D. Tsuei, C. Felser and S. S. Parkin, *Proc. Nat.l Acad. Sci. U. S. A* **113**, 11148-11151 (2016).
- [67] X. Meng, F. Quenneville, F. Venne, E. Di Mauro, D. Işık, M. Barbosa, Y. Drolet, M. M. Natile, D. Rochefort, F. Soavi and C. Santato, *J. Phys. Chem. C* **119**, 21732-21738 (2015).
- [68] H. Kalhori, M. Coey, I. Abdolhosseini Sarsari, K. Borisov, S. B. Porter, G. Atcheson, M. Ranjbar, H. Salamati and P. Stamenov, *Sci. Rep.* **7**, 12253 (2017).
- [69] T. Onozato, Y. Nezu, H. J. Cho and H. Ohta, *AIP Adv.* **9**, 025122 (2019).
- [70] T. Onozato, H. J. Cho and H. Ohta, *Jpn. J. Appl. Phys.* (2019).

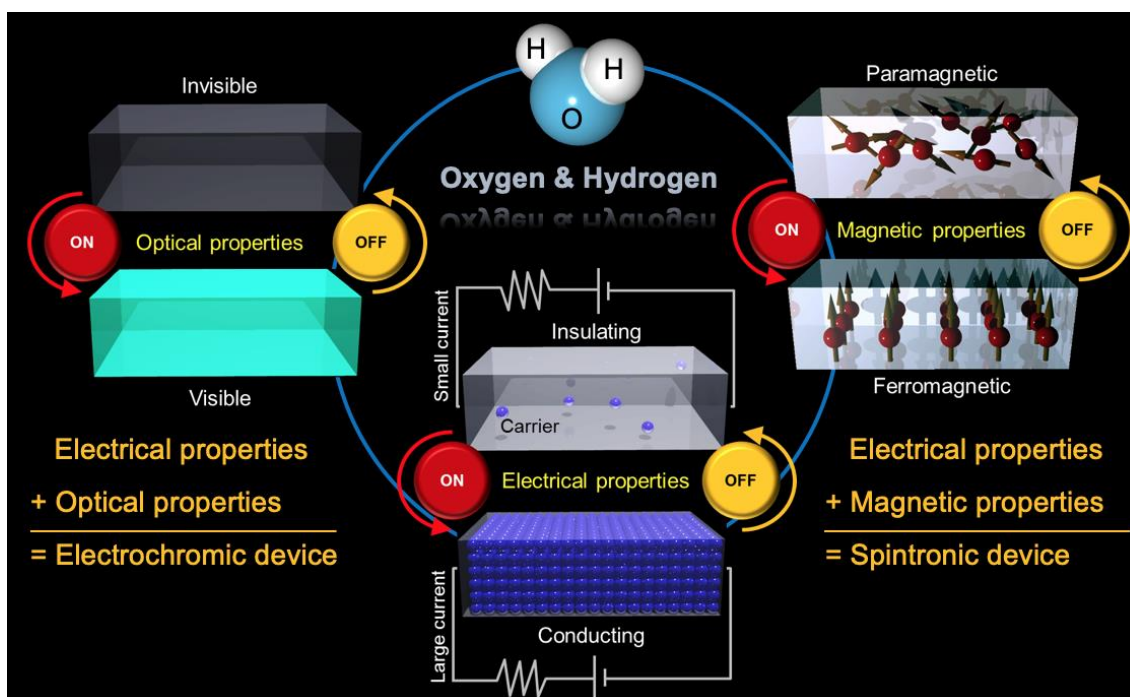


Figure 1. Research concept of functional oxide devices. Water contains oxygen (OH^-) and hydrogen (H^+). OH^- is a strong oxidizing agent and H^+ is a strong reducing agent for TMOs. The electro-optical and electromagnetic properties of TMOs can be controlled by using water. Such a combination of electrochemistry and oxide electronics will lead to advanced multifunctional devices, such as electrochromic and spintronic devices based on TMOs.

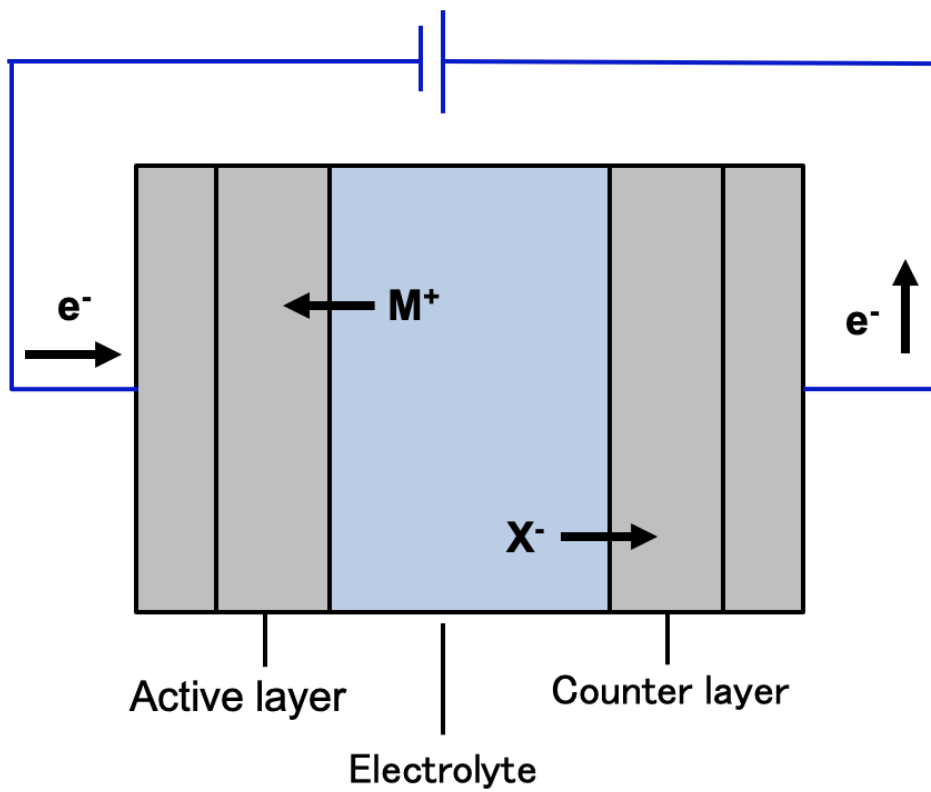


Figure 2. Basic structure of electrochromic device (electrochromic display type). The electrochromic devices are composed of electrochromic active layer, electrolyte layer, and counter layer, which are sandwiched by two transparent electrodes (usually ITO).

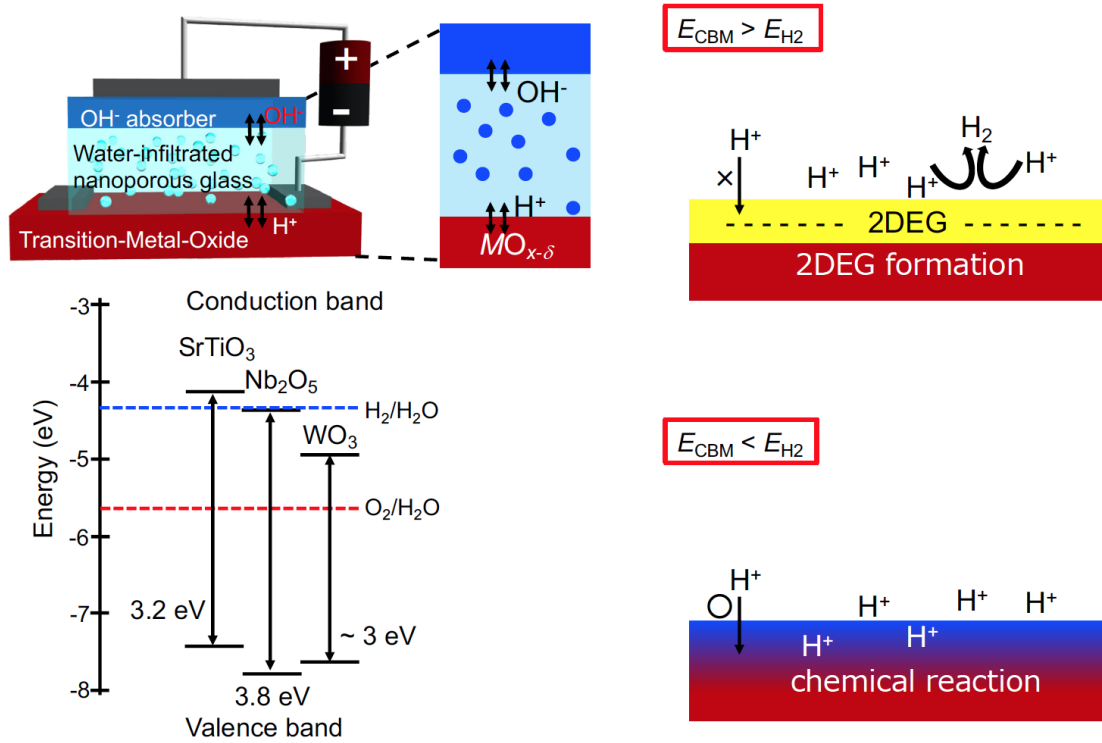


Figure 3. Reactions in the active layer in contact with the thin CAN film. When the conduction band minimum (CBM) of the active layer material located in contact with the CAN is higher than the hydrogen generation level (eg SrTiO₃, KTaO₃) H⁺ attracted to the active layer surface does not react with the active layer, forms an electric double-layer capacitor, and accumulates high-density carriers on the active layer electrode surface¹⁰. On the other hand, when the CBM of the active layer material is lower than the hydrogen generation level, proton H⁺ enters the active layer material and causes an electrochemical reaction.

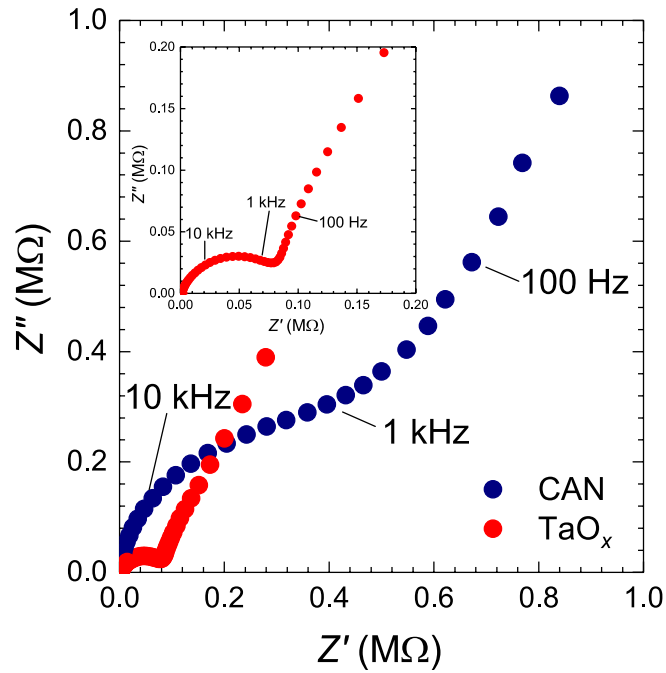


Figure 4. Cole-Cole plot of the TaO_x and CAN film measured at RT. The calculated conductivity of TaO_x and CAN was 125 nS cm^{-1} and 24 nS cm^{-1} , respectively. Ionic-conductivity of TaO_x film was 5 times higher than CAN film. Since the CAN film has a nano-porous structure, but tantalum oxide film has a nano-pillar array structure, it is easy to imagine that the nanopillar array structure has higher ionic-conductivity than the nano-porous structure.

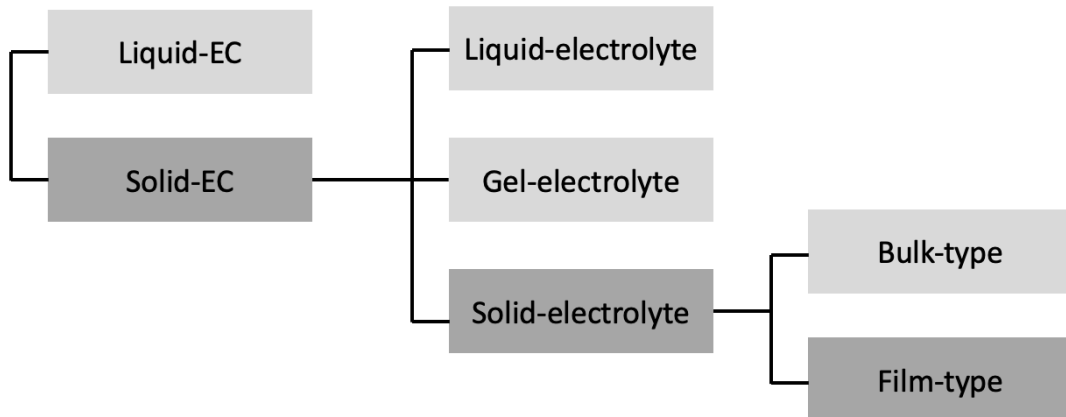


Figure 5. Classification of electrochromic devices. The electrochromic material can be classified liquid or a solid type. When the electrochromic material is liquid type, the electrolyte material, and the counter material should be a liquid state. When the electrochromic material is solid type, there are three types of electrolyte layers: solid, gel and liquid type. When the electrolyte layer is a liquid type, there are two types of a counter layer, a liquid type, and a solid type. When the electrolyte layer is a solid type, the counter layer is a solid type. Solid-type counter layers include thin-film types fabricated by vacuum processes, and thick-film (bulk) types formed by coating methods.

1. General Introduction



Figure 6. Electrochromic windows used on Boeing 787 aircraft.

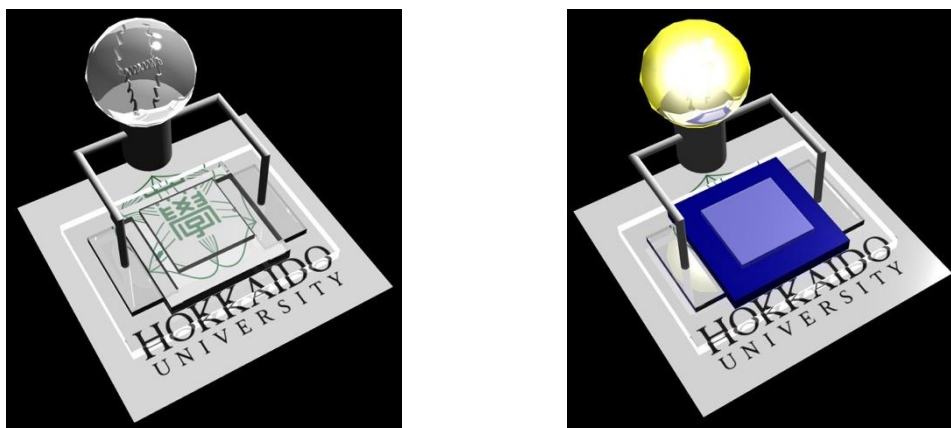


Figure 7. Concept of an electrochromic metal-insulator switching device (ECT: Electrochromic transistor). The device can be switched from a colorless transparent / insulator state (left panel) to a dark blue / metallic state (right panel) simultaneously by electrochemical protonation / deprotonation at RT in air.

2. Experimental Method

2.1. Pulsed Laser Deposition (PLD) method

The electrochromic transistors were fabricated using pulse laser deposition method (PLD) technique, which is one of the physical vapor deposition methods for thin-film deposition. The pulsed laser deposition (PLD) method irradiates a target material placed in a vacuum with focused laser light (pulse laser), and excited species (ion, neutrality) are generated with photochemical reaction, which is accompanied by explosive vaporization since the energy of the laser is very large. The vaporized atoms/molecules are sprayed on the substrate above and deposited as a thin film. **Figure 1** shows the apparatus for PLD, whereas **Figure 2** shows the ablation in the deposition chamber. The excited chemical species generated in this way are called plume, which can collide with the gas in the chamber. Therefore, in the PLD method, the laser settings (power, optical path etc.) as well as the vacuum conditions can affect the deposition process. The laser irradiates the material that forms the thin film called the target.

Detailed reaction kinetics of PLD method involves a high-intensity light-matter interaction. At first, the laser beam with a pulse width of about 10 ns is focused and irradiated on the target surface, and a very high power density (laser fluence) can be obtained at the peak of one pulse. Therefore, thin films can be formed relatively easily even with a target material having a high melting point as long as the material absorbs laser light. Since the high degree of vacuum required by other PVD methods is not required, the oxygen partial pressure in the reaction system can be high, and the oxygen

2. *Experimental Method*

content in the thin film can easily be adjusted with the partial pressure of oxygen. In addition, film growth can be controlled with the number of pulses ^{1, 2}. As only the outermost surface of the target can be instantaneously ablated with the pulse laser, solid state diffusion in the target is negligible, and the composition of the target is uniformly transferred to the film. In-situ observation is also possible using RHEED (reflection high-energy electron diffraction). Unlike molecular beam epitaxy (MBE) and sputtering, which continuously deposit films, the PLD method can independently control nucleation and surface migration. These features of PLD are suitable for the growth of thin films of multi-component complex oxides or metal oxides having a high melting point.

Thin film growth with the PLD method is performed through three main processes. The first step is the ablation of the target by the laser light, which chemically excites the species in the target. The ablated target forms vapor, reaches the substrate, and finally forms the film. During the ablation process, the interaction between the laser beam and the solid surface varies greatly depending on the laser intensity, pulse width, wavelength, and solid absorption coefficient. For example, when a short-wavelength laser source is used, since the absorption coefficient of solid is usually large, most of the light is absorbed in the vicinity of the target surface, and the temperature near the target surface rises sharply. Within a few nanoseconds, the target surface exceeds the melting point, causing a rapid expansion, and atoms/molecules are ejected out of the target surface. These atoms/molecules also absorb laser light and are re-excited to become thermal plasma as the temperature rises again. The high-energy plasma instantaneously expands in the vacuum and leaves the surface.

2. Experimental Method

In gas phase processes, the behavior of atoms ejected from the target surface is determined by the laser energy and the chamber atmosphere. In oxygen atmospheres, shock waves are generated from the target surface during the ablation. As the atmospheric gas pressure increases, a stronger shock wave is generated, and the atoms are compressed. A hot, compressed oxygen gas layer is formed at the front of the shock wave, and a formation of monoxide is promoted in that layer by the collision between the plume and the oxygen gas. Since the mean free path of atoms decreases as the oxygen pressure increases, the distance between the target and the substrate also plays a major role in the film formation.

In order to produce a high-quality thin film, it is important to control the crystal growth process on the substrate. Thin film crystal orientation can be controlled by controlling thermodynamics (thin film growth temperature) and kinetics (flux of atoms). Using RHEED during the film growth, the growth temperature and kinetics can systematically be controlled, and *in situ* observation of crystal growth modes (three-dimensional growth, layer-by-layer growth, step-flow growth) is possible.

2.2. Structural characterization

2.2.1. XRD measurement

X-ray diffraction (XRD), which is one of the most essential characterization tools in the research field, enables detailed structural characterizations of the material according to Bragg's law:

$$2d\sin\theta = n\lambda$$

Where d is the lattice distance, θ is the Bragg angle, 2θ is the diffraction angle, and n is an integer. The path difference between the X-rays scattered on two adjacent atomic planes is expressed by $2d\sin\theta$. When this path difference is an integral multiple of the incident X-ray wavelength λ (the X-ray wavelength used in this study is the $\text{CuK}_{\alpha 1}$ line $\lambda \approx 1.54 \text{ \AA}$), constructive interference occurs between the scattered waves. In other words, a strong diffraction peak can be obtained when the Bragg condition is satisfied. Essential crystallographic information on the order of nanometer can be obtained as wavelengths on the order of sub- \AA to \AA can be used. In this study, high resolution X-ray diffractometer ATX-G of Rigaku Co., Ltd was used to characterize the films. This X-ray diffractometer has five measurement axes and can perform in diffraction scans in three dimensions. For example, out-of-plane measurement is performed for the out-of-plane orientation of the thin film, and in-plane measurement is performed when information within the thin film is needed. In addition, if the films are thin and has a flat surface smooth, the X-ray penetrates into the sample surface at a shallow angle with an out-of-plane $2\theta/\omega$ arrangement. From the interference fringes measured between 0° and 10° , the density,

2. Experimental Method

thickness, and surface roughness of the thin film can be obtained. This is called the X-ray reflectivity measurement (XRR measurement).

2.2.2. Scanning transmission electron microscopy (STEM)

In this study, scanning transmission electron microscopy (STEM) was used to observe the structure of the fabricated device. STEM is a technique that can obtain structural information from a thin specimen by irradiating an electron beam and analyzing the transmitted electrons. Inelastically and elastically scattered electrons are also collected by the objective lens, and electron diffraction (ED) micrographs are formed, which give information on crystallography, orientation, and lattice defects etc. In the bright field (BF) mode, an objective aperture is inserted in the back focal plane of the objective lens (the surface from which the electron diffraction pattern appears), and only the central transmitted wave is passed through the aperture to form an image. Diffraction does not occur in this mode, so the contrast of the image is the brightest. Conversely, a region that satisfies the Bragg condition is imaged with a dark contrast. This observation mode is suitable for comprehensive structural characterization of the entire specimen. In this study, amorphous material was used, and the crystal structure was observed from the electron diffraction microscopy³⁻⁵.

Figure 3 shows electron diffraction images of single crystal, polycrystal, and amorphous Si. In the case of single crystal, a diffraction pattern according to the symmetry of the crystal is observed. In the case of polycrystals, concentric patterns (Debye rings) are formed instead of spots due to the random crystal orientations. In case

2. Experimental Method

of amorphous Si, since there is no crystal structure, a clear diffraction spot cannot be observed, and a concentric halo pattern is formed, which is blurred.

2.2.3. Optical property measurement

In this study, light transmittance was used to measure the changes in the optical properties during the operation of the fabricated electrochromic device. For a certain wavelength, the following expression holds among the absorptance A_λ , the reflectance R_λ , and the transmittance T_λ of the material.

$$A_\lambda + R_\lambda + T_\lambda = 1$$

Since the electrochromic device fabricated in this study has an element size on the order of μm , the light transmittance was measured with MSV-5200 JASCO with an irradiation light size of $100 \mu\text{m}$, manufactured by JASCO Corporation.

2.3. Operating mechanism

In this section, the operating mechanism of this electrochromic transistors is described. **Figure 4** shows the operating mechanism of electrochromic transistor. Above all, this device is a current-driven type electrochemical device, not conventional field-effect transistor. Firstly, when a positive voltage is applied to the top gate electrode, the water-infiltrated nanoporous thin film (solid-electrolyte) acts as a dielectric, and the a-WO₃ and NiO thin film surfaces are slightly metalized due to electrostatic effects and then form an electric double-layer capacitor. Consequently, proton H⁺ and hydroxide ion OH⁻ inside the solid-electrolyte thin film are attracted to the a-WO₃ and NiO thin film

2. Experimental Method

surfaces, respectively. Protonation ($\text{WO}_3 + x\text{H}^+ + xe^- \Leftrightarrow \text{H}_x\text{WO}_3$)⁶ and hydroxylation ($\text{NiO} + \text{OH}^- \Leftrightarrow \text{NiOOH} + e^-$)^{7, 8} make the a-WO₃ thin film metalized and colored. Conversely, when a negative voltage is applied, the a-WO₃ thin film becomes an insulator and decolorized by deprotonation as the hydroxide ions and hydrogen ions move back to the nanoporous film.

References

- [1] Y. Zhang, B. Feng, H. Hayashi, C.-P. Chang, Y.-M. Sheu, I. Tanaka, Y. Ikuhara and H. Ohta, *Nat. Commun.* **9**, 2224 (2018).
- [2] Y. Zhang, B. Feng, H. Hayashi, T. Tohei, I. Tanaka, Y. Ikuhara and H. Ohta, *J. Appl. Phys.* **121**, 185102 (2017).
- [3] E. Okunishi, H. Sawada and Y. Kondo, *Micron* **43**, 538-544 (2012).
- [4] H. Ohta, S. Kim, Y. Mune, T. Mizoguchi, K. Nomura, S. Ohta, T. Nomura, Y. Nakanishi, Y. Ikuhara, M. Hirano, H. Hosono and K. Koumoto, *Nature Materials* **6**, 129-134 (2007).
- [5] N. Shibata, S. D. Findlay, Y. Kohno, H. Sawada, Y. Kondo and Y. Ikuhara, *Nature Physics* **8**, 611-615 (2012).
- [6] J. Vondrák and J. Bludská, *Solid State Ionics* **68**, 317-323 (1994).
- [7] I. C. Faria, R. Torresi and A. Gorenstein, *Electrochim. Acta* **38**, 2765-2771 (1993).
- [8] C. G. Granqvist, in *Handbook of Inorganic Electrochromic Materials*, edited by C. G. Granqvist (Elsevier Science B.V., Amsterdam, 1995), pp. vii-viii.

2. Experimental Method

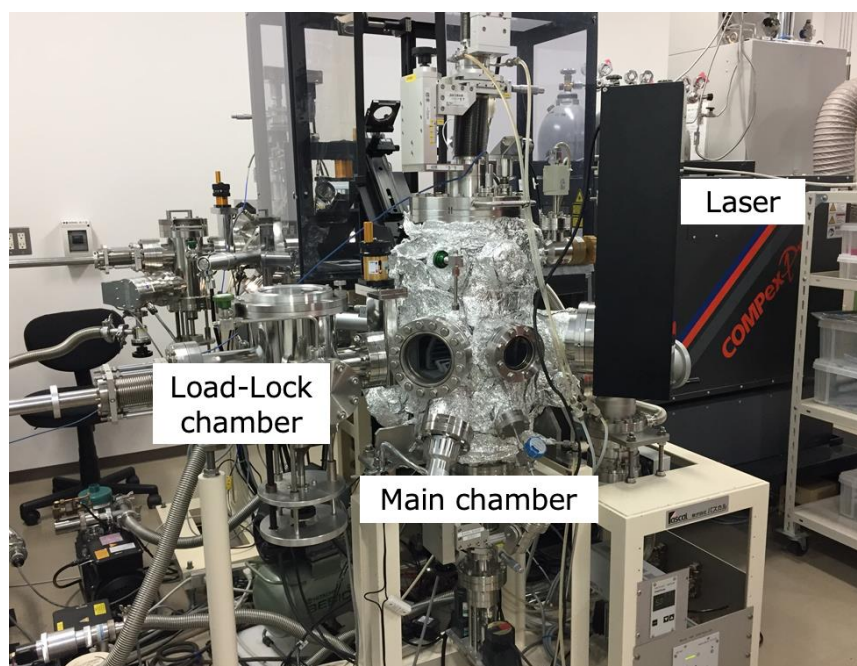


Figure 1. Overview of PLD system

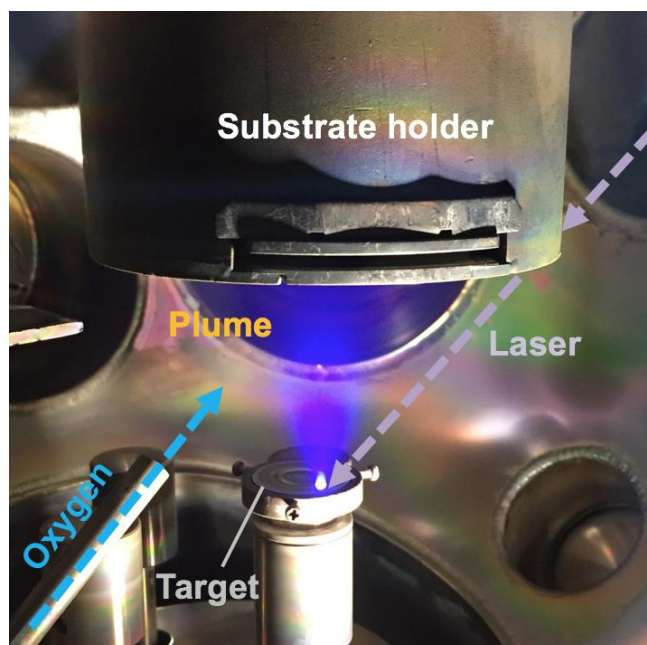


Figure 2. Film deposition with PLD equipment

2. Experimental Method

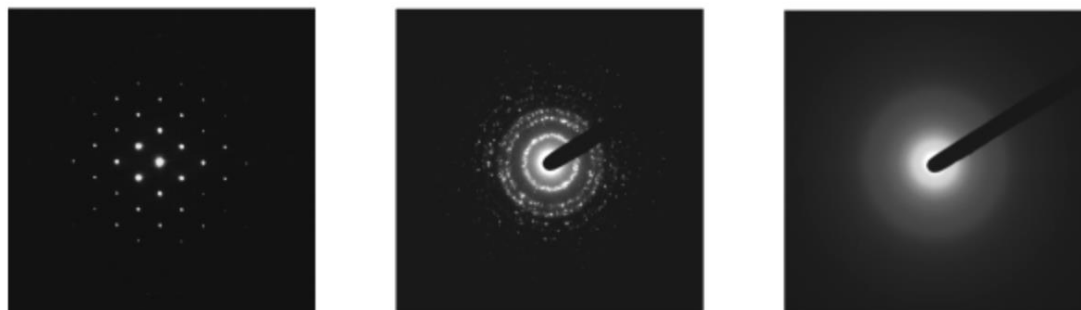


Figure 3. Electron diffraction (ED) pattern images of single crystal Si (left panel), polycrystalline Si (center panel), and amorphous Si (right panel). The single crystal, polycrystalline, and amorphous structures show a discrete spot, ring, and halo patterns, respectively.

2. Experimental Method

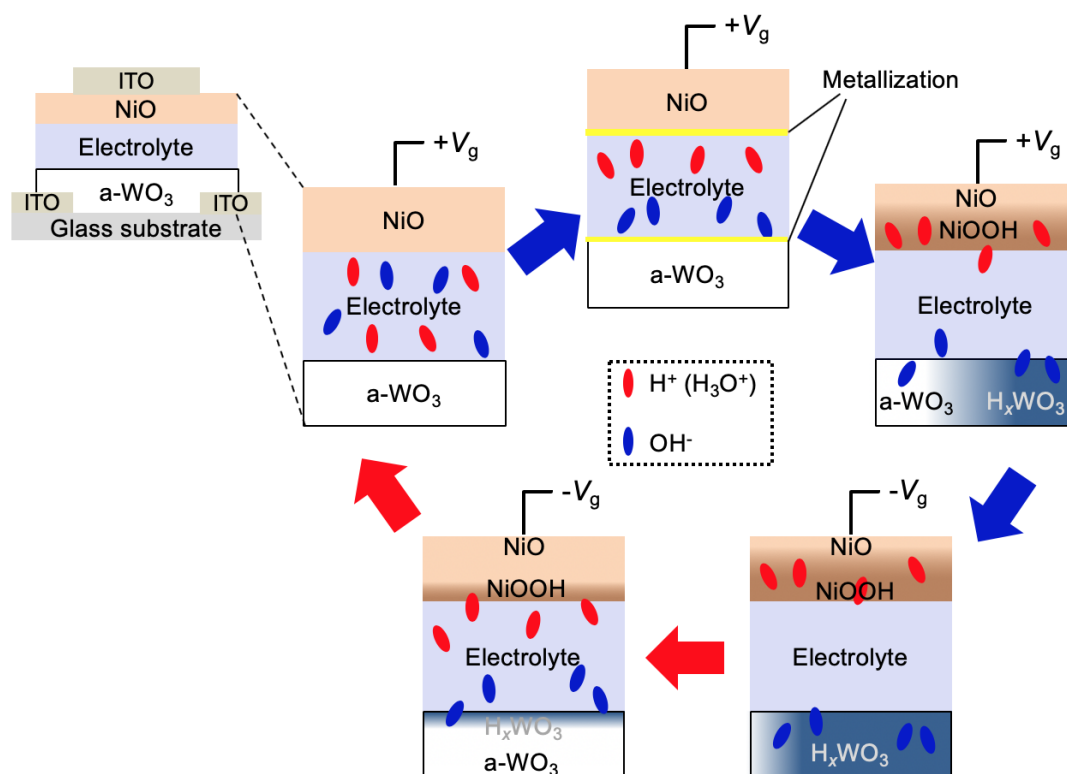


Figure 4. Schematic image of Electrochromic transistor operating mechanism.

3. A transparent electrochromic metal-insulator switching device with three-terminal transistor geometry

3.1. Introduction

A transparent electrochromic metal-insulator (EC-MI) switching device that can be electrically switched from a colorless transparent insulator to a colored metallic conductor would be ideal for future energy-saving technologies, such as advanced smart-windows. In the OFF state, such transparent EC-MI switching device fully transmits visible light, whereas it does not transmit light in the ON state. Furthermore, the device is switched from insulator to conductor at the same time, which can function as an ON/OFF power switch for other electronic devices.

Among many potential electrochromic materials, tungsten trioxide (WO_3)¹ shows the greatest suitability for the EC-MI switching devices. Stoichiometric WO_3 is a transparent insulator with a bandgap (E_g) of 2.6–3.0 eV² and has a defect perovskite-type structure with space group $P2_1/n$, in which A-sites in the ABO_3 lattices are vacant³. If the vacant A-sites become occupied by protons (H^+), *i.e.* the formation of tungsten bronze, it becomes an electrical conductor and opaque to visible light following the valence-state change of W ion from W^{6+} to W^{5+} ⁴. Thus, the protonation/deprotonation of WO_3 is promising method for the realization of simultaneous electrical switching between colorless/colored and insulating/conducting states, as shown in **Figure 1**.

Various types of WO_3 -based EC devices have been actively developed for applications in energy-saving smart windows^{5,6}; however, their MI switching behavior

3. A transparent electrochromic metal-insulator switching device with three-terminal transistor geometry

has not been utilized with EC switching simultaneously because of their two-terminal structure, which involves a parallel-plate electrode configuration. Electrostatic charge modulation using three-terminal thin-film transistors (TFTs)^{7, 8} on a WO₃ thin film could be used to realize simultaneous EC-MI switching; however, it remains difficult to fully switch their coloring state because of limitations associated with the carrier-doping range and modifiable thickness⁹. Several researchers have developed liquid-electrolyte gated transistors^{10, 11} and successfully demonstrated EC-MI switching of WO₃. However, because these devices require liquid electrolytes, they are less practical for application, which depends on effective sealing.

In this chapter, a *liquid-leakage-free* transparent EC-MI switching device is demonstrated. **Figure 2a.** schematically illustrates the device structure, which has a typical three-terminal TFT-type structure composed of an active channel, a gate insulator, and source-drain-gate electrodes. An amorphous a-WO₃ thin film was used as the active channel layer because EC switching of a-WO₃ film prepared on glass substrate at room temperature (RT) has been previously reported¹². The gate insulator consists of an a-12CaO·7Al₂O₃ (a-C12A7) thin film with nanoporous structure (calcium aluminate with nanopore, CAN)^{13, 14}. It should be noted that the film porosity of CAN film can be controlled by oxygen pressure (P_{O_2}) during thin-film deposition at RT (porous structure can be observed at $P_{O_2} > 1$ Pa), and the nanopores with average diameters of 10–20 nm connect with each other when the pore fraction reaches ~30%, leading to the percolation conduction of water in the CAN film. Since C12A7 is a hydroscopic material, water vapor in air is automatically absorbed into the CAN film, like a solid sponge, via the capillary

3. *A transparent electrochromic metal-insulator switching device with three-terminal transistor geometry*

action in the interconnected nanopores. Therefore, water electrolysis can be used in the solid gate insulator. A NiO/ITO (indium tin oxide) bilayer film was used as the transparent gate electrode, and ITO thin films were used as the transparent source and drain electrodes.

The device with leakage-free water can be considered as the nanosized electrochemical cell with a nanogap parallel plate structure, which enables the high electric-field application for ion migration and effective protonation/deprotonation of the a-WO₃ layer (Fig. 2b). Thus, a gate voltage (V_g) application induces water electrolysis in the CAN film and produces H⁺ and OH⁻ ions move for protonating the a-WO₃ layer ($\text{WO}_3 + x\text{H}^+ + xe^- \rightarrow \text{H}_x\text{WO}_3$)¹⁵ and hydroxylating the NiO layer ($\text{NiO} + \text{OH}^- \rightarrow \text{NiOOH} + e^-$),¹⁶ respectively. The NiO counter layer is expected to work as the OH⁻ absorber, which maintains a better electrochemical balance and should improve the reversibility as well as the reproducibility of device operation. Alternative positive and negative V_g applications induce the reversible protonation/deprotonation of a-WO₃ layer, switching it from a transparent insulator to a dark blue conductor. The present EC-MI switching device with the two combined functions of color changing as a display and electrical switching as a transistor in one device can be reversibly operated at RT without sealing; thus, it may be suitable for a wide-range application in future energy-saving technologies, such as advanced smart-windows.

3. A transparent electrochromic metal-insulator switching device with three-terminal transistor geometry

3.2. Experimental

Device fabrication

The present liquid-leakage-free transparent EC-MI switching device (active channel area: 400 μm in width and 800 μm in length) was fabricated on an alkaline-free glass substrate (Corning[®] EAGLE XG[®], substrate size: 10 \times 10 \times 0.7 mm) by pulsed laser deposition (PLD) using stencil masks. All thin-film fabrications were conducted at room temperature (RT), where a KrF excimer laser (wavelength of 248 nm, repetition rate of 10 Hz) was used to ablate ceramic target disks. Firstly, 20-nm-thick metallic ITO films (resistivity, $\rho = 1.0 \text{ m}\Omega \text{ cm}$ at RT) were deposited at O_2 pressure (P_{O_2}) of 4 Pa as the transparent source and drain electrodes. Then, a- WO_3 channel layer was deposited under P_{O_2} of 7 Pa, where the deposition rate of a- WO_3 film was 6 nm min^{-1} . 300-nm-thick CAN gate insulator was deposited under P_{O_2} of 5 Pa to make CAN film with nanoporous structure^{13, 14}. NiO (20 nm) / ITO (20 nm) bilayer film was deposited as the transparent gate electrode on the CAN film surface, where the nanopores in the CAN film is small enough to prevent the NiO/ITO film penetrate into the CAN film and reach the a- WO_3 layer during the deposition. The density of a- WO_3 film was 5.96 g cm^{-3} , evaluated by grazing incidence X-ray reflectivity, which corresponds to 82% of ideal density of a WO_3 crystal (7.29 g cm^{-3})¹⁷. The AC conductivity of the CAN film was $3.7 \times 10^{-8} \text{ S cm}^{-1}$ at RT, slightly less than the $5.6 \times 10^{-8} \text{ S cm}^{-1}$ of ultrapure water¹⁸.

3. *A transparent electrochromic metal-insulator switching device with three-terminal transistor geometry*

Structural characterization

Crystallinity of the fabricated thin films were investigated with grazing incidence X-ray diffraction analyses (Cu $K\alpha_1$, ATX-G, Rigaku Co.), which revealed that all oxide layers were amorphous expect for the polycrystalline NiO film. Cross-sectional thin-film samples for TEM observations were prepared by focused-ion-beam (FIB) micro-sampling technique, in which the multilayer structure region of the TFTs was cut and thinned by FIB (FB-2000A, HITACHI) to obtain samples for the cross-sectional observation. The cross-sectional microstructure and electron diffraction pattern of the a-WO₃ devices were examined by high-resolution TEM and STEM (JEM-ARM200F, 200 kV, JEOL Ltd.).

Electrical and optical property measurements

Gate current (I_g) was measured between the gate and source electrodes during the V_g application using a source measurement unit (Keithley 2450). Since electrochemical reaction during the device operation was non-volatile, the electrical and optical properties were measured after turning the V_g off. R_s were measured by the d.c. four-point probe method (van der Pauw configuration). For the retention time dependence of I_g and R_s (Figs. 5a and 5b), I_g was measured at 1 s intervals while R_s was measured at intervals of 20 s at +3 V, 10 s at +5 V, 5 s at +10 V, 5 s at -3 V, 2 s at -5 V, and 1 s at -10 V, respectively. Thermopower (S) was measured by creating a temperature difference (ΔT) of ~4 K in the film using two Peltier devices, where the temperatures of both sides of a-WO₃ channel layer were monitored by two thermocouples. The thermo-electromotive force (ΔV) and

3. A transparent electrochromic metal-insulator switching device with three-terminal transistor geometry

ΔT were simultaneously measured, and the S -values were obtained from the linear slope of the ΔV - ΔT plots. Optical transmission spectra were measured by UV-Vis/NIR microscope with the light irradiation area of 100 μm in diameter (MSV-5200, JASCO). The relative humidity value during the device performance test was $\sim 30\%$ at 25 $^{\circ}\text{C}$. Since the present device exhibits electrochemically reversible operation, the water in CAN gate insulator is not be lost during the device operation, and the degradation of CAN due to gas penetration is prevented. However, it is likely that the humidity in air slightly affect the device operation, but it is beyond the scope of this dissertation and should be tested in future.

3.3. Result

Figure 2c shows a bright-field scanning transmission electron micrograph (BF-STEM, heavy atoms appear dark) of the cross-section of the resultant device, which reveals the multi-layer structure of ITO (20 nm)/NiO (20 nm)/CAN (300 nm)/a-WO₃ (80 nm) on the glass substrate. Several bright spots with diameters of 10–20 nm are clearly seen in the CAN film, indicating the presence of high-density nanopores in the CAN film. **Figure 2d** shows the selected-area electron diffraction patterns of the NiO/ITO gate electrode layer (top) and the a-WO₃ channel layer (bottom). A broad halo was observed for the a-WO₃ film, confirming the amorphous structure. Meanwhile, a ring diffraction pattern was seen for NiO/ITO film, originating from polycrystalline nature of NiO film,

3. A transparent electrochromic metal-insulator switching device with three-terminal transistor geometry

which was also confirmed by the grazing incidence X-ray diffraction measurements of each thin film.

Metal-insulator switching

The MI switching of the device was investigated by measuring the sheet resistance (R_s) and thermopower (S) at RT after applying V_g for a given amount of time. **Figure 3a** plots R_s as a function of applied $\pm V_g$ at RT. Firstly, a positive V_g up to +10 V was applied to protonate the a-WO₃ channel (left panel, application time of 20 s each), and then negative V_g up to -10 V was applied to deprotonate the a-H_xWO₃ channel (right panel, application time of 10 s each). The initial a-WO₃ channel was insulating, but the reduction in R_s of more than six orders of magnitude was observed upon the application of positive V_g ; the R_s exponentially decreased from 17 M Ω sq.⁻¹ at +2 V, plateaued at $\geq +8$ V, and stabilized at $R_s = 30 \Omega$ sq.⁻¹ when V_g was +10 V. It should be noted that the protonated a-H_xWO₃ channel was stable under ambient and vacuum conditions at RT, confirming the non-volatile device operation. Subsequently, by applying negative V_g up to -10 V, R_s clearly recovered, reaching an insulating state (6.8 M Ω sq.⁻¹).

Then the S for a-WO₃ channel protonated and deprotonated at each $\pm V_g$ was measured since S is a good measure to evaluate the changes in the electronic-structure resulting from carrier doping (protonation)^{19,20}. **Figure 3b** shows the relationship between S and $1/R_s$ for the device at RT. S -values were always negative, indicating that the channel layer is an n-type conductor. The $|S|$ linearly decreased from 47 μ V K⁻¹ to 11 μ V K⁻¹ in a logarithmic scale against $1/R_s$ and the linear relation was observed regardless of the

3. A transparent electrochromic metal-insulator switching device with three-terminal transistor geometry

direction of the electrochemical reaction, suggesting that protonation of the a-WO₃ channel provides electrons to the conduction band. The derivative of the electronic density of states (DOS) with respect to the energy near the Fermi energy (E_F), $\left[\frac{\partial \text{DOS}(E)}{\partial E} \right]_{E=E_F}$, becomes moderate, resulting in the consequent reduction of $|S|$ -values.

Figure 3c shows the results of repeated R_s switching of the a-WO₃ channel at various V_g : ± 3 , ± 5 , and ± 10 V. For protonation ($+V_g$), the V_g application time was 20 s while the that for deprotonation ($-V_g$) was 10 s. Clear cyclability of R_s switching was observed at each V_g , and the R_s modulation ratio was largely dependent on the magnitude of V_g ; the ON/OFF ratio was $\sim 10^3$ at ± 3 V, $\sim 10^4$ at ± 5 V, and $\sim 10^6$ at ± 10 V. Reversible and stable R_s switching with large ON/OFF ratios occurred rapidly on the order of seconds.

The device operation is considered to be largely dependent on time-scaled processes consist of ionic polarization in water, electric double layer formation, electrochemical reaction, and H⁺ diffusion in the a-WO₃ channel upon the V_g applications. Among these processes, the rate-determining step has been reported to be the surface reaction process ^{21,22}. Therefore, the discrepancy between the application times of $+V_g$ (protonation) and $-V_g$ (deprotonation) should originate from the activation barrier of the surface reaction. For example, the diffusion of H⁺ in and out of the active layer has different interfacial resistances ²³, which can be seen from the different gate current flowing in the device at the V_g with the same magnitude and a different sign (**Fig. 6a** and **6b**). In addition, the V_g -dependent ON/OFF ratio of the R_s modulation (**Fig. 3c**) suggests that the diffusivity of H⁺

3. A transparent electrochromic metal-insulator switching device with three-terminal transistor geometry

along the out-of-plane direction can be controlled by V_g , and the entire channel is protonated by applying $V_g \geq 8$ V.

Electrochromic switching

Next, the EC switching of the device was evaluated. **Figure 4a** shows the optical transmission spectra of the device in the initial state (black line) and protonated states at +3 V (red line), +5 V (green line), and +10 V (blue line). The transmission (T) of the device greatly changed by upon the application of $+V_g$. The initial device was, to some extent, transparent in the visible region. After protonation, T at $\lambda = 700$ nm was reduced to 24% that of the initial state (transmission decrease of 35%). The inset shows the optical micrographs of the device at the initial and protonated states (+10 V); the color clearly changes from transparent colorless to opaque dark blue, as can be seen in the $L^*a^*b^*$ color space (**Fig. 4b**), confirming the optical modulation of the a-WO₃ channel. **Figure 5** shows the optical reflectance of each state. From optical transmittance and reflectance, the absorption coefficient of the device in the initial state (black line) and protonated states at +3 V (red line), +5 V (green line), and +10 V (blue line) are shown **Figure 6**. The absorption near the wavelength of 800 nm gradually increases with increasing applied voltage. This result indicates plasma absorption occurred by free-electron carrier increase. Thus, simultaneous EC-MI switching was realized in the device. It should be noted that there is no direct evidence for the hydroxylation of NiO to form NiOOH in this device, which should also affect the optical transmission spectra as NiO changes its color from transparent to deep brown by hydroxylation²⁴. However, considering that the no gas

3. A transparent electrochromic metal-insulator switching device with three-terminal transistor geometry

formation was observed in this device, it is likely that the OH^- ions were indeed absorbed by the NiO counter layer. In fact, many reports on the hydroxylation of NiO with aqueous solutions and their effect on electrochromic devices ²⁴. Therefore, NiO should play as OH^- absorption layer but further confirmation is necessary.

3.4. Discussion

To clarify the device operation mechanism, the relationship between the flowing current and R_s of the a-WO₃ channel under various V_g was investigated. Figures 6a and 6b summarize the retention-time (t) dependence of the gate current (I_g) along with R_s for the a-WO₃ channel under V_g of ± 3 , ± 5 , and ± 10 V, where $+V_g$ was initially applied for protonation (Fig. 6a) and $-V_g$ was subsequently applied for deprotonation (Fig. 6b). I_g and R_s were measured during and after the V_g application, respectively. Upon the application of $+V_g$ (Fig. 6a), $+I_g$ always increased with t (the I_g at $+10$ V showed an irregular jump, exponentially increased, and then eventually saturated) with the R_s simultaneously decreasing, indicating the electrochemical protonation of the a-WO₃ channel. On the other hand, upon the application of $-V_g$ (Fig. 6b), $-I_g$ decreased with t at each $-V_g$ while R_s simultaneously increased due to electrochemical deprotonation. This observation suggests the following device operation mechanism. The $+V_g$ application first accumulates charge carriers at the film surface via electrostatic field effect with small $+I_g$, resulting in the formation of parallel-plate capacitor. The electric field then starts to reach the channel surface, and a further $+V_g$ application causes dissociation of H^+ and OH^- ions,

3. A transparent electrochromic metal-insulator switching device with three-terminal transistor geometry

which are attracted to the top and bottom film surface. This should be primary origin of the significant increase in I_g at the initial stage. The H^+ and OH^- ions diffuse from the surface to bulk region of a- WO_3 film and NiO counter layer, where the conductivity improvement of each layer exponentially increases the I_g .

Next, the variation in R_s of the a- WO_3 channel with respect to applied electron density was compared (Fig. 6c). The applied electron density (Q) was estimated as, $Q = \frac{C}{s \times q}$ where C is total coulomb amount calculated from the integral value of the I_g-t plots in Fig. 6a and 6b, s is the surface area of a- WO_3 channel, and q is elementary charge, respectively. During protonation ($+V_g$ application), R_s steeply decreased with increasing Q up to $1.2 \times 10^{17} \text{ cm}^{-2}$ ($\equiv 1.5 \times 10^{22} \text{ cm}^{-3}$) and then remained unchanged with further electron injection. In contrast, during deprotonation ($-V_g$ application), R_s increased moderately until Q reached up to $1.3 \times 10^{17} \text{ cm}^{-2}$ ($\equiv 1.6 \times 10^{22} \text{ cm}^{-3}$) and then sharply switched to an insulating state. The changes in R_s with Q seems to be different during the protonation and deprotonation processes, which should be attributed to the inhomogeneous H^+ distribution in a- H_xWO_3 channel along the out-of-plane direction and the H^+ -concentration dependent activity (chemical potential) of H^+ transport²⁵. The critical Q for MI switching of the a- WO_3 channel corresponds to the ideal Q value ($1.3 \times 10^{17} \text{ cm}^{-2}$) required for the achieving 100 % protonation/deprotonation in the a- WO_3 , which agrees with the theoretical value that can be predicted according to the following reaction: $WO_3 + H^+ + e^- \rightleftharpoons HWO_3$ (the Q is estimated by $Q = \frac{\rho \times T}{M} \times N_A$, where M is

3. *A transparent electrochromic metal-insulator switching device with three-terminal transistor geometry*

molar mass of WO_3 , ρ is the film density, T is the film thickness, and N_A is Avogadro constant, respectively).

The activation energy (E_a) of the electrical conductivity for the fully protonated $\text{a-H}_x\text{WO}_3$ channel calculated from the R_s - T measurements (Fig. 7) was $E_a = 4.3 \times 10^{-3}$ eV. This was an order of magnitude smaller than $E_a = 5.0 \times 10^{-2}$ eV reported for the $\text{a-H}_x\text{WO}_3$ film ($x = 0.32$)²⁶. Since the E_a is a function of x due to the band filling, the lower E_a in the a-WO_3 channel layer supports that it is effectively protonated by water-electrolysis with the application of high electric-field in the present TFT-type structure. In addition, R_s decreased and increased along the same universal trend under all values of V_g . This indicates that all provided electrons were used for electrochemical protonation and deprotonation of the a-WO_3 channel, obeying Faraday's laws of electrolysis. These confirm that the device operation can be controlled by the current density.

3.5 Conclusion

The present device with leakage-free water can be reversibly switched from a colorless transparent insulator to a colored metallic conductor in a short amount of time (~ 10 s). In the ON state, visible light cannot transmit through the device, whereas the visible light can fully be transmitted in the OFF state. The device can also function as an ON/OFF power switch for other electronic devices. As the device is mainly composed of amorphous oxide films, which can be deposited at RT. This means that there are almost no limitations on the substrate material selection for the device fabrication. Moreover, the

*3. A transparent electrochromic metal-insulator switching device
with three-terminal transistor geometry*

device can be operated without sealing due to the liquid-leakage-free CAN gate insulator. These features are suitable for the development of large-area devices and mass production; thus, the present device may find practical application in future energy-saving technologies, such as advanced smart windows.

3. A transparent electrochromic metal-insulator switching device
with three-terminal transistor geometry

References

- [1] C. G. Granqvist, *Sol. Energy Mater. Sol. Cells* **60**, 201-262 (2000).
- [2] P. P. González-Borrero, F. Sato, A. N. Medina, M. L. Baesso, A. C. Bento, G. Baldissera, C. Persson, G. A. Niklasson, C. G. Granqvist and A. F. d. Silva, *Appl. Phys. Lett.* **96**, 061909 (2010).
- [3] H. Zheng, J. Z. Ou, M. S. Strano, R. B. Kaner, A. Mitchell and K. Kalantar-zadeh, *Adv. Funct. Mater.* **21**, 2175-2196 (2011).
- [4] P. G. Dickens and M. S. Whittingham, *Quarterly Reviews, Chemical Society* **22**, 30-44 (1968).
- [5] C. G. Granqvist, *Sol. Energy Mater. Sol. Cells* **92**, 203-208 (2008).
- [6] S. K. Deb, *Sol. Energy Mater. Sol. Cells* **92**, 245-258 (2008).
- [7] H. Ohta and H. Hosono, *Mater. Today* **7**, 42-51 (2004).
- [8] E. Fortunato, P. Barquinha and R. Martins, *Adv. Mater.* **24**, 2945-2986 (2012).
- [9] C. H. Ahn, A. Bhattacharya, M. Di Ventra, J. N. Eckstein, C. D. Frisbie, M. E. Gershenson, A. M. Goldman, I. H. Inoue, J. Mannhart, A. J. Millis, A. F. Morpurgo, D. Natelson and J.-M. Triscone, *Rev. Mod. Phys.* **78**, 1185-1212 (2006).
- [10] M. J. Natan, T. E. Mallouk and M. S. Wrighton, *J. Phys. Chem.* **91**, 648-654 (1987).
- [11] P. Barquinha, S. Pereira, L. Pereira, P. Wojcik, P. Grey, R. Martins and E. Fortunato, *Adv. Electron. Mater.* **1** (2015).
- [12] S. K. Deb, *The Philosophical Magazine: A Journal of Theoretical Experimental and Applied Physics* **27**, 801-822 (1973).
- [13] H. Ohta, Y. Sato, T. Kato, S. Kim, K. Nomura, Y. Ikuhara and H. Hosono, *Nat. Commun.* **1**, 118 (2010).
- [14] H. Ohta, T. Mizuno, S. Zheng, T. Kato, Y. Ikuhara, K. Abe, H. Kumomi, K. Nomura and H. Hosono, *Adv. Mater.* **24**, 740-744 (2012).
- [15] J. Vondrák and J. Bludská, *Solid State Ionics* **68**, 317-323 (1994).
- [16] X. H. Xia, J. P. Tu, J. Zhang, X. L. Wang, W. K. Zhang and H. Huang, *Sol. Energy Mater. Sol. Cells* **92**, 628-633 (2008).
- [17] S. Tanisaki, *J. Phys. Soc. Jpn.* **15**, 566-573 (1960).
- [18] T. S. Light, S. Licht, A. C. Bevilacqua and K. R. Morash, *Electrochem Solid St* **8**, E16-E19 (2005).
- [19] T. Katase, K. Endo and H. Ohta, *Physical Review B* **90** (2014).

3. *A transparent electrochromic metal-insulator switching device
with three-terminal transistor geometry*

- [20] T. Katase, K. Endo, T. Tohei, Y. Ikuhara and H. Ohta, *Adv. Electron. Mater.* **1** (2015).
- [21] M. A. Vannice, M. Boudart and J. J. Fripiat, *J. Catal.* **17**, 359-& (1970).
- [22] Y. Xi, Q. Zhang and H. Cheng, *J. Phys. Chem. C* **118**, 494-501 (2013).
- [23] Z. K. Luo, Z. S. Ding and Z. H. Jiang, *J. Non-Cryst. Solids* **112**, 309-313 (1989).
- [24] C. G. Granqvist, in *Handbook of Inorganic Electrochromic Materials*, edited by C. G. Granqvist (Elsevier Science B.V., Amsterdam, 1995), pp. vii-viii.
- [25] R. S. Crandall, P. J. Wojtowicz and B. W. Faughnan, *Solid State Commun.* **18**, 1409-1411 (1976).
- [26] R. S. Crandall and B. W. Faughnan, *Phys. Rev. Lett.* **39**, 232-235 (1977).

3. A transparent electrochromic metal-insulator switching device with three-terminal transistor geometry

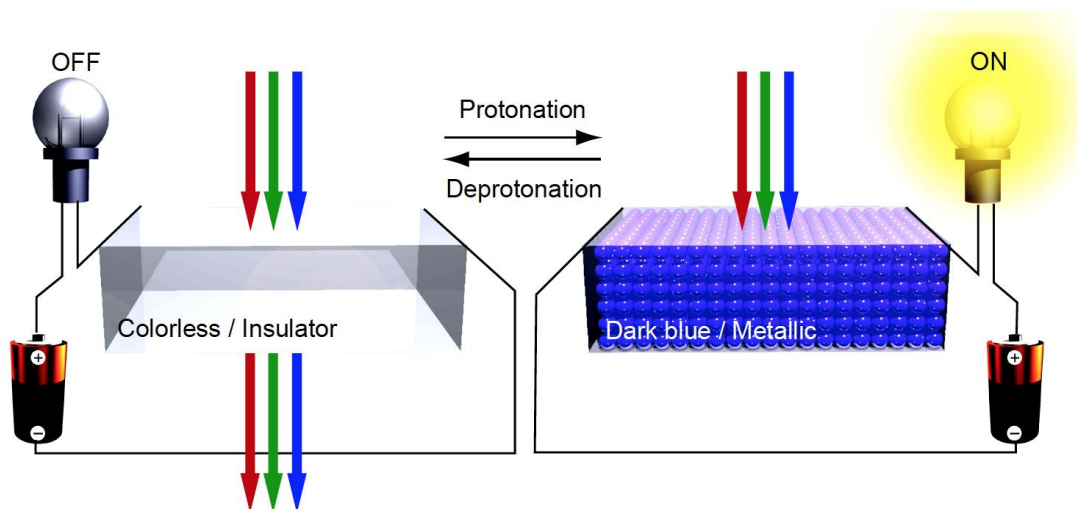


Figure 1. Concept of an electrochromic metal-insulator switching device. The device can be switched from a colorless transparent/insulator state to a dark blue/metallic state simultaneously using electrochemical protonation / deprotonation at RT in air. In the ON state, the visible light cannot be transmitted through the device, whereas it can be fully transmitted in the OFF state. Furthermore, the device can function as an ON/OFF power switch for other electronic devices as well. Such a device would be useful for advanced smart window application.

3. A transparent electrochromic metal-insulator switching device with three-terminal transistor geometry

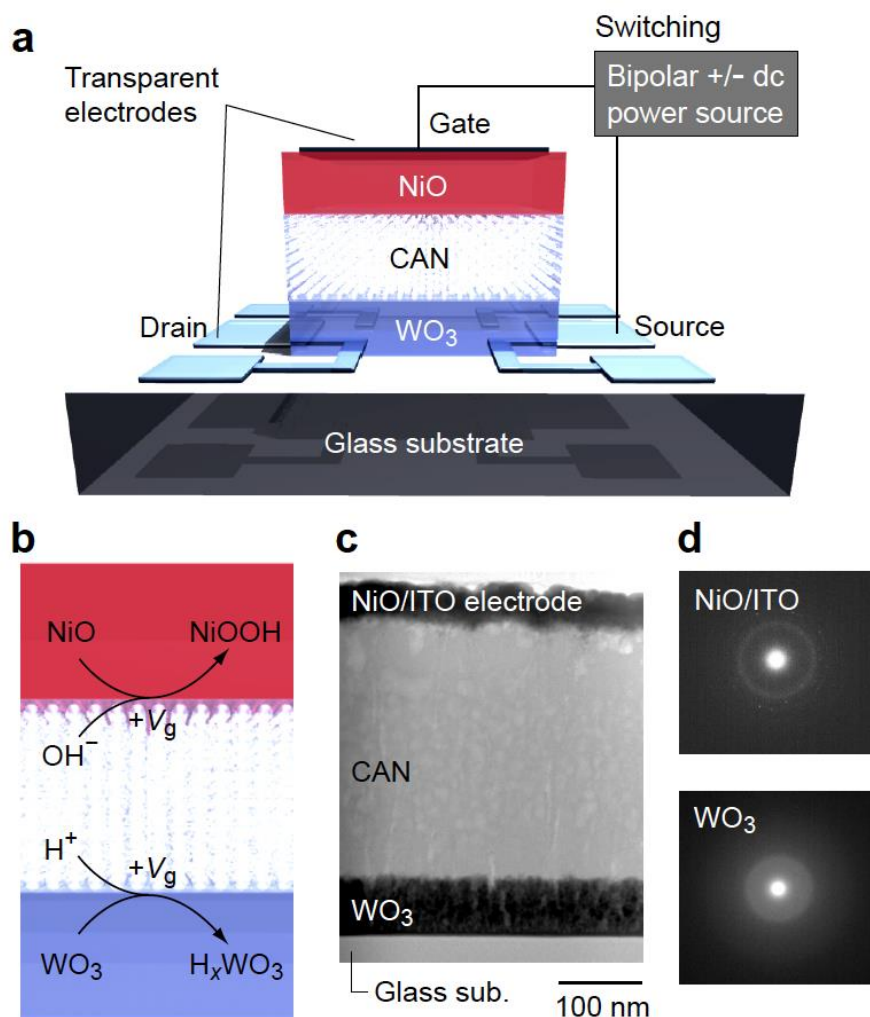


Figure 2. A transparent EC-MI switching device. (a) Schematic device structure of three-terminal TFT-type device, composed of a-WO₃ (80 nm), CAN (300 nm), and NiO (20 nm) / ITO (20 nm) layers. Transparent ITO thin films are used for all the electrodes. (b) Device operation mechanism. During the positive V_g application, protonation of a-WO₃ layer and hydroxylation of NiO layer occur simultaneously. Conversely, a-H_xWO₃ and NiOOH return to a-WO₃ and NiO during the negative V_g application. (c) Cross-sectional BF-STEM image of the device. Trilayer structure is clearly seen. Many bright spots in the CAN layer from the nanopores can be observed, which is fully occupied with water. (d) Selected area electron diffraction patterns of NiO/ITO layer (upper) and a-WO₃ layer (lower).

3. A transparent electrochromic metal-insulator switching device with three-terminal transistor geometry

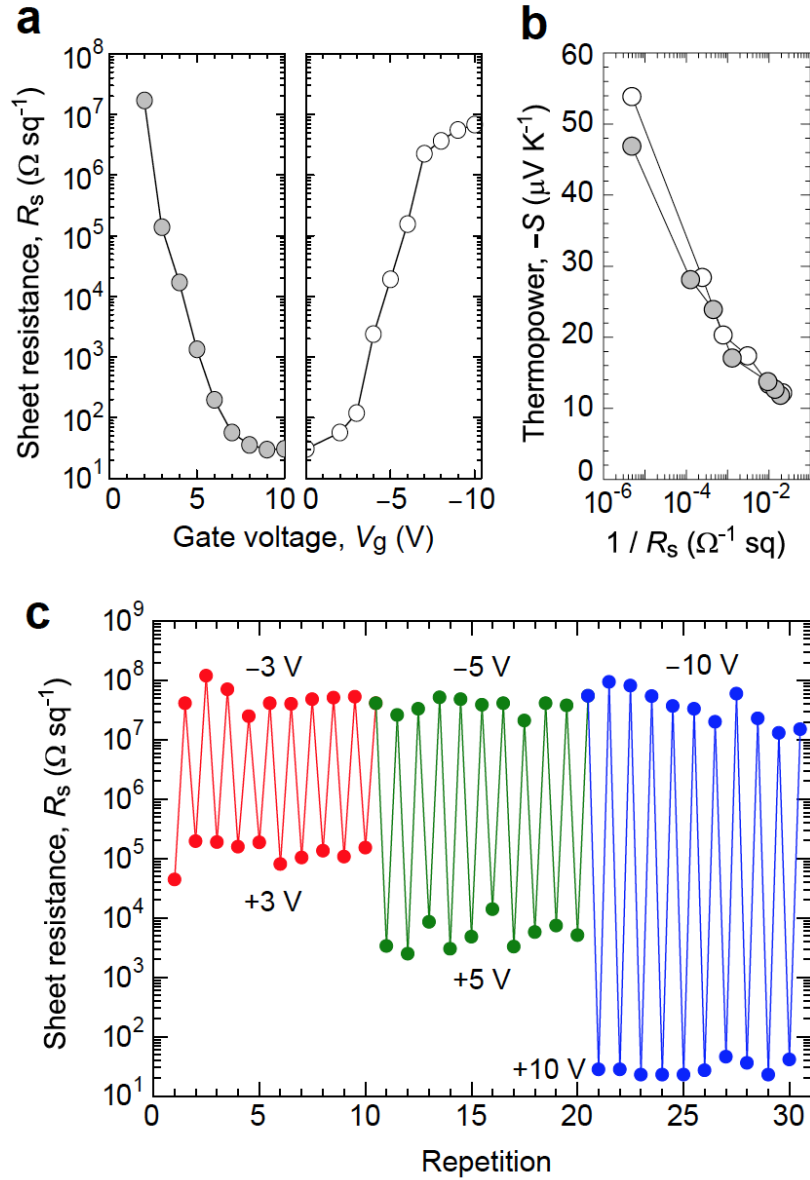


Figure 3. Metal-insulator switching of the transparent EC-MI switching device. (a) Sheet resistance (R_s) as a function of applied V_g in the a-WO₃ layer. R_s values were measured after V_g application, where positive V_g up to +10 V was applied for protonation of a-WO₃ film (left panel, V_g application time of 20 s each), and then negative V_g up to -10 V was applied for deprotonation of a-H_xWO₃ film (right panel, V_g application time of 10 s each). (b) Thermopower (S) as a function of $1/R_s$ at RT. The linear relation between $-S$ and logarithmic $1/R_s$ was reversible and reproducible. (c) Repetitive switching test by applying various $V_g = \pm 3, \pm 5,$ and ± 10 V. The R_s modulation ratio can be controlled to be $\sim 10^3$ for ± 3 V, $\sim 10^4$ for ± 5 V, and $\sim 10^6$ for ± 10 V, respectively.

3. A transparent electrochromic metal-insulator switching device with three-terminal transistor geometry

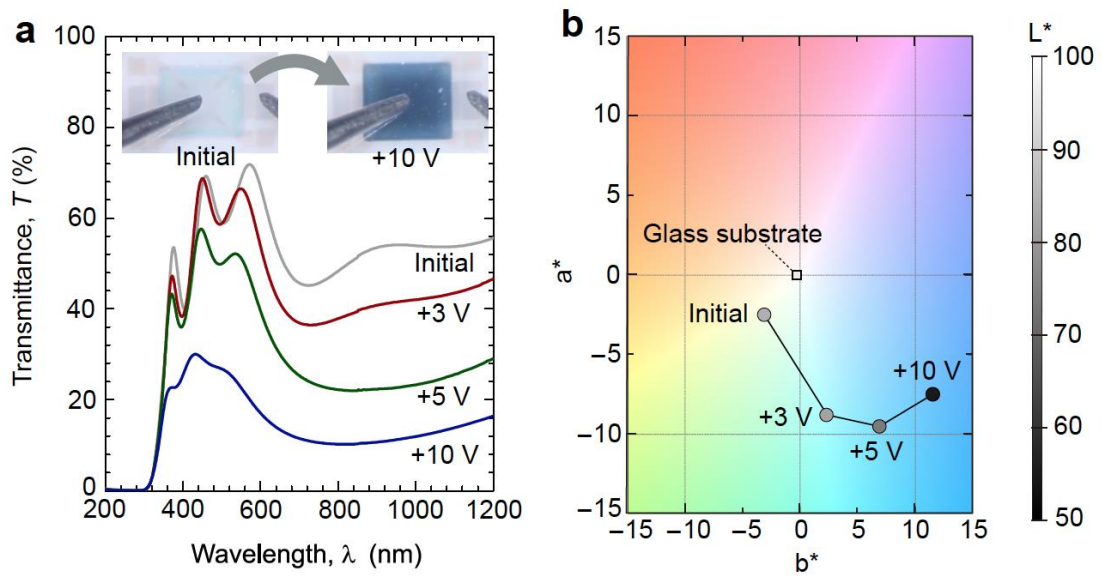


Figure 4. Electrochromic switching of the transparent EC-MI switching device. (a) Optical transmission spectra of the device. Significant decrease of the transmission is seen with increasing V_g . The inset shows the optical micrographs of the device; after the application of $V_g = +10$ V, the device became opaque / dark blue (right), whereas the device was colorless transparent at the initial state (left). (b) $L^*a^*b^*$ color space plot of the device at each state in (a).

3. A transparent electrochromic metal-insulator switching device with three-terminal transistor geometry

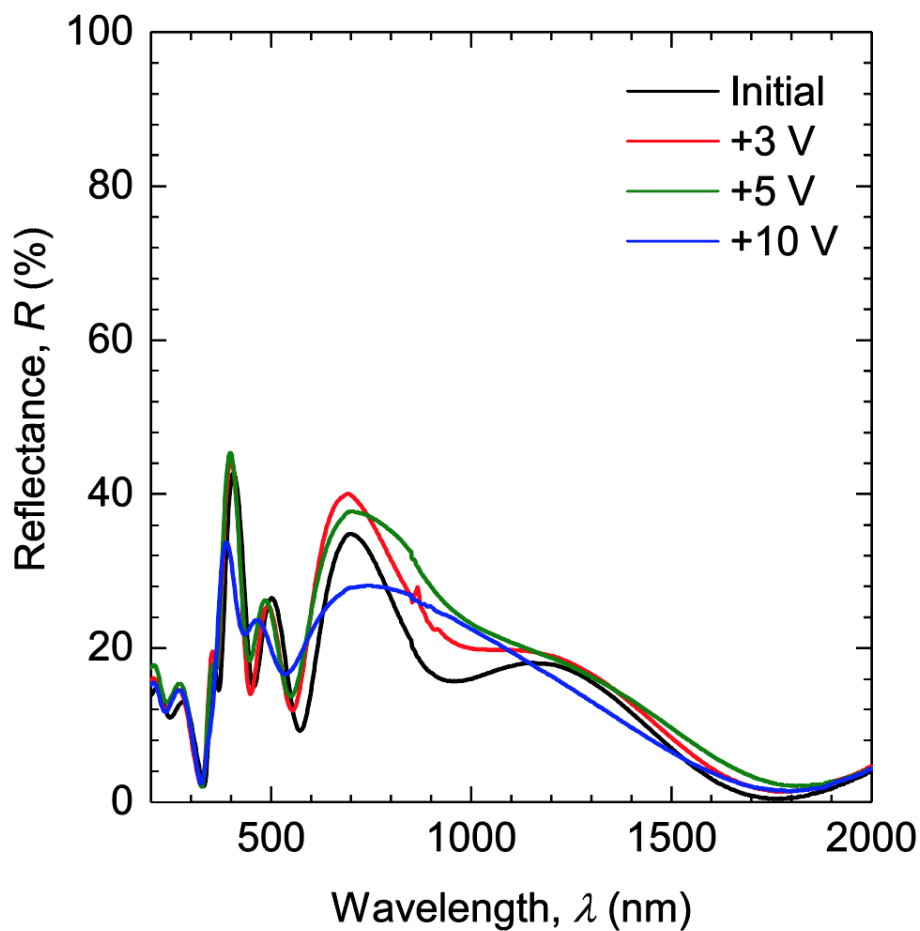


Figure 5. Optical reflectance spectra of the device at each voltage application state.

3. A transparent electrochromic metal-insulator switching device with three-terminal transistor geometry

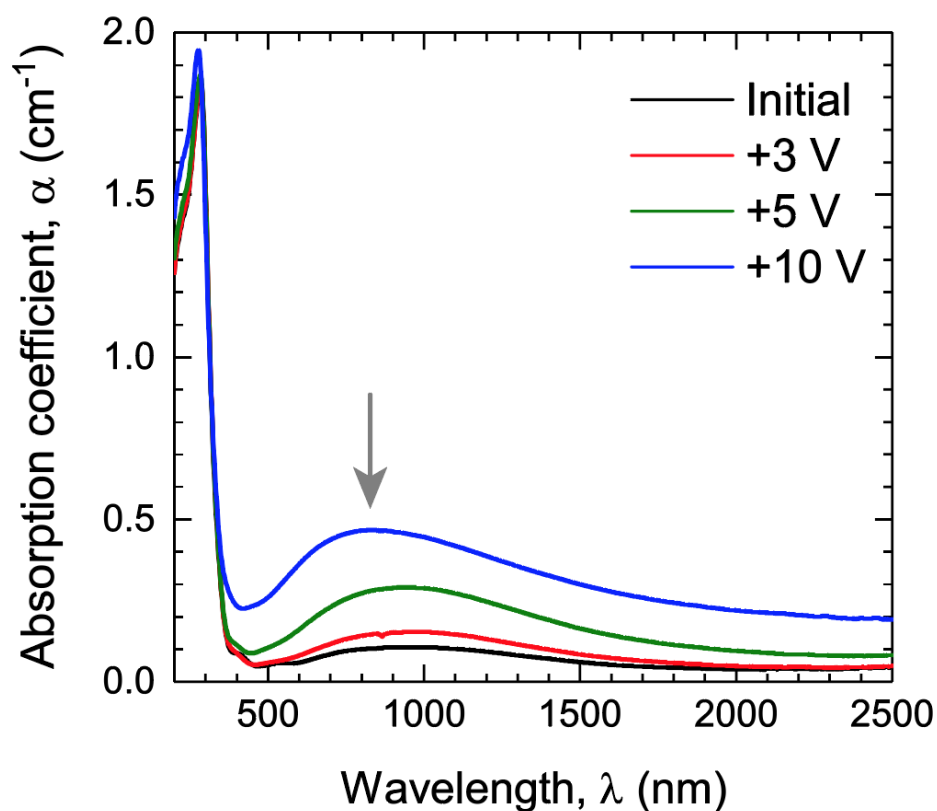


Figure 6. The absorption coefficient of the device in the initial state (black line) and protonated states at +3 V (red line), +5 V (green line), and +10 V (blue line) from optical transmittance and reflectance. The absorption near the wavelength of 800 nm gradually increases with increasing applied voltage.

3. A transparent electrochromic metal-insulator switching device with three-terminal transistor geometry

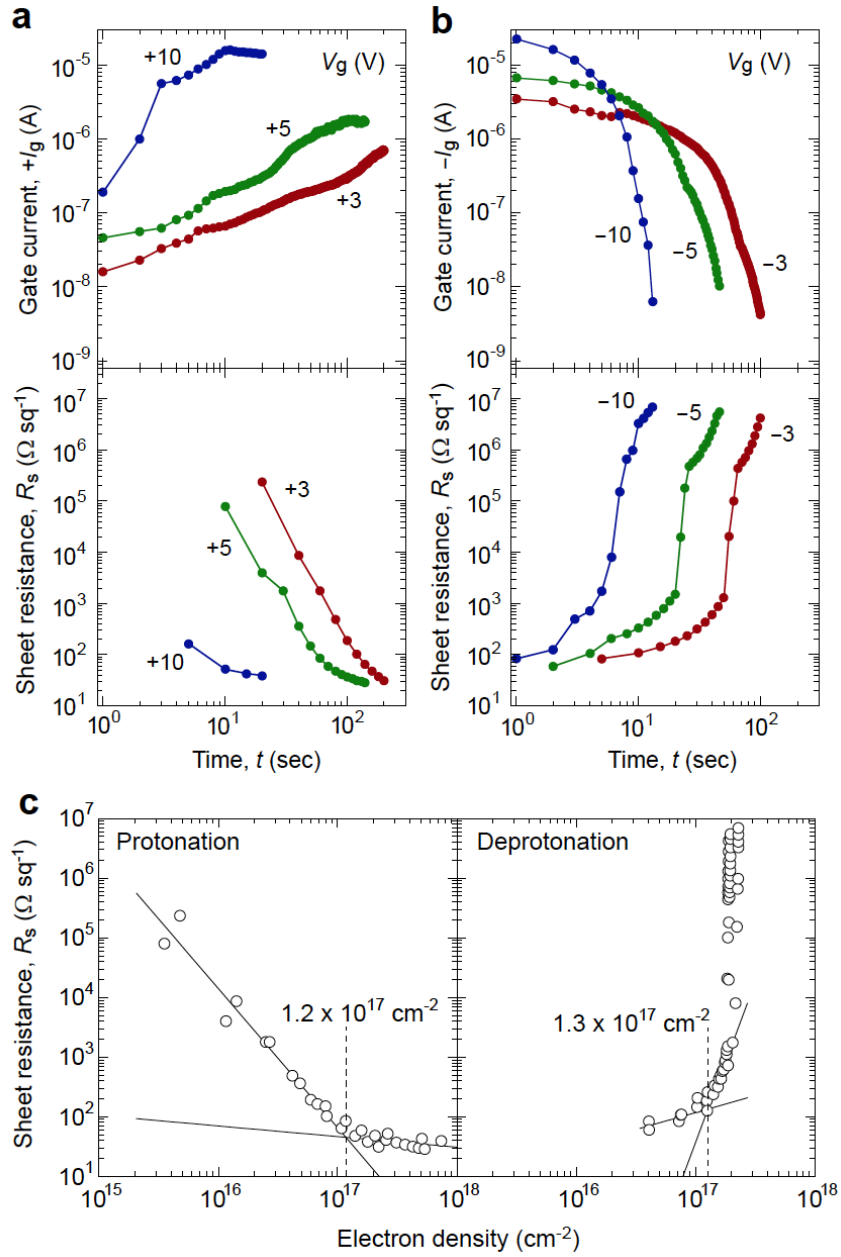


Figure 6. Switching mechanism of the transparent EC-MI switching device. (a, b) Retention time (t) dependence of gate current (I_g , upper) and sheet resistance (R_s , lower) under application of various $\pm V_g$'s from 3, 5, and 10 V, where (a) $+V_g$ was initially applied for protonation and (b) $-V_g$ was subsequently applied for deprotonation. (c) Electron-density (Q) dependence of R_s under application of the various values of V_g . Q was calculated as the integrated value of the I_g - t plots in (a, b). The universal changes in R_s are presented by the black lines. The critical Q of protonation and deprotonation was 1.2 – $1.3 \times 10^{17} \text{ cm}^{-2}$, which corresponds well with the ideal Q ($1.3 \times 10^{17} \text{ cm}^{-2}$) required for the 100 % protonation / deprotonation reaction of $\text{WO}_3 + \text{H}^+ + \text{e}^- \rightleftharpoons \text{HWO}_3$.

3. A transparent electrochromic metal-insulator switching device with three-terminal transistor geometry

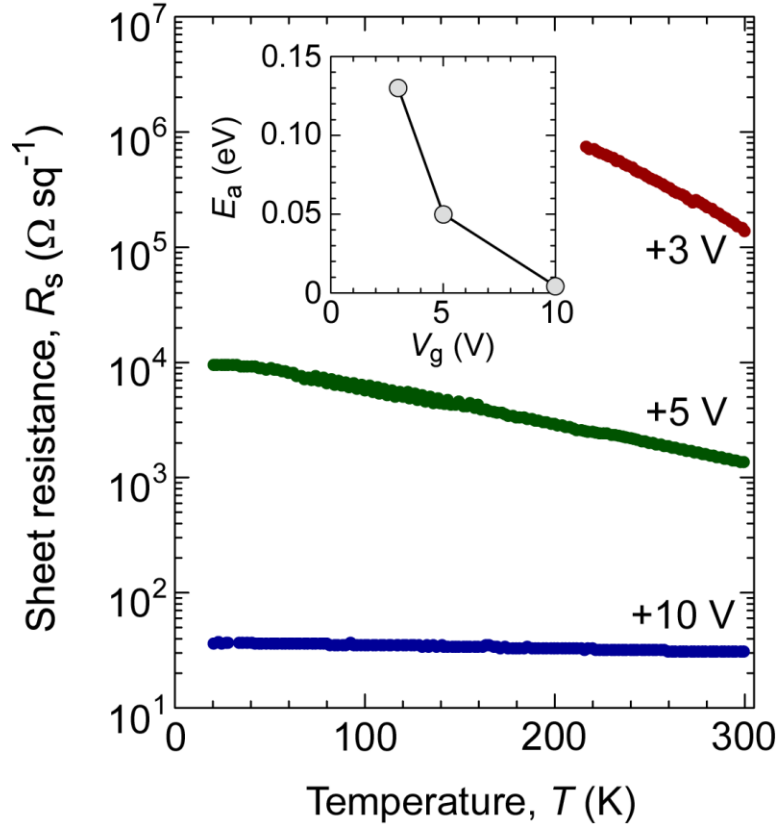


Figure 7. Temperature dependence of sheet resistance (R_s) for the a-WO₃ channel layer of the device protonated at $V_g = +3$ V, +5 V, and +10 V applied for 20 s. All the R_s - T curves showed semiconduct behaviors; the exponential increase of R_s was observed with decreasing temperature. This is consistent with other reports on the electrical conductivity of a-WO₃, a-H_xWO₃, and a-Na_xWO₃ films, which follows the variable range hopping model between localized electronic states. The inset shows the activation energy (E_a), estimated from $\ln(1/R_s)$ vs. $1000/T$ relation at 300–200 K range. The E_a largely decreased from 1.3×10^{-1} eV to 4.3×10^{-3} eV, and the R_s - T curve at +10 V showed almost no temperature dependence. Considering that the minimum E_a of electrochemically prepared a-H_xWO₃ film ($x = 0.32$) was reported to be 5.0×10^{-2} eV, the proton concentration is much higher in the a-H_xWO₃ channel of the present device.

4. Fast operation of a WO₃-based solid-state electrochromic transistor

4.1. Introduction

Recently, electrochromic transistors (ECTs), which can function as both electrochromic displays (ECDs) and three terminal transistors, have attracted increasing attention as advanced memory devices because ECTs have advantages against conventional data storage devices, which can store 1 bit information of 0 or 1 ^{1,2}. For example, WO₃-based ECTs drastically change their resistance when the gate voltage is positive. At the same time, the color of the ECT turns from almost colorless transparent into dark blue. Thus, ECTs can store the information of electrical resistance and color simultaneously in a non-volatile manner^{2,3}.

Although many EC materials including organic materials are known⁴⁻⁶, inorganic WO₃ has become popular as the active material of ECT devices because WO₃-ECTs show large on/off current switching ratio and intense color change, and there are many reports on WO₃-based ECT that investigated the structure phase transition and metal-insulator transition using a liquid electrolyte and an epitaxial WO₃ film⁷⁻¹⁰. Furthermore, amorphous WO₃-ECT was prepared even on a paper substrate². Very recently, neuromorphic transistor^{11,12}, which imitated synaptic movements, has been developed using WO₃-ECTs. Some studies utilized solid electrolyte to build WO₃-ECTs^{3,13}, which have advantage over liquid electrolyte based WO₃-ECTs because they are free from the leakage issues.

ECTs are quite different compared to conventional field effect transistors (FET). In

4. Fast operation of a WO_3 -based solid-state electrochromic transistor

the case of FET, charge carrier accumulation from to the electrostatic field generates the conducting channel. On the other hand, for ECTs, the chemical composition in the active channel must be changed by the electrochemical reaction to modulate the resistance. Therefore, the operating speed of ECTs is much slower than conventional FETs; the operation speed of WO_3 -based ECT devices with liquid electrolyte are around 20 seconds². In addition, the operation of the all-solid-state WO_3 based-ECT requires at least 1 min^{3, 13}.

In order to overcome this issue, the device structure was considered. In contrasts to the ECTs, ECDs can usually be operated within several milliseconds^{6, 14}. **Figure 1** schematically shows the structural difference between an ECD (**Fig. 1a**) and an ECT (**Fig. 1b**). Both devices are composed of WO_3 , electrolyte, and NiO, which are sandwiched by two transparent conducting oxides (TCOs). In ECD, its parallel plate electrode configuration and uniform distribution of electric field allow its operating speed to be much faster than that of ECT, of which the electrode configuration is asymmetric. However, while the ECT is much slower, its three-terminal configuration can utilize the changes in the resistance, which is not possible in the ECD configuration. This dilemma can perhaps be resolved if the structures of ECD and ECT are combined.

This chapter demonstrates a fast operation of a solid-state WO_3 -ECT. A three terminal thin film solid-state ECT with a parallel plate electrode configuration was fabricated as shown in **Fig. 1c**. In order to realize a symmetric electrode configuration, a thin ZnO layer was inserted as a thin TCO. This approach greatly reduced the operation time to less than 1s at ± 3 V application while keeping the ON/OFF ratio of ~ 30 . This present ECT structure

advances the current ECT's technology and may be implemented in advanced memory technology utilizing both electrochromism and transistor operation.

4.2. Experimental

The ECT devices were fabricated on an alkaline-free glass substrate by pulsed laser deposition (PLD) with KrF excimer laser (248 nm, 10 Hz) using stencil masks as shown in **Figs. 2a** and **2b**. All film fabrication processes were conducted at room temperature. At first, 30-nm-thick ZnO films (Electrical conductivity: $\sim 50 \text{ S cm}^{-1}$) were deposited on the substrate as the bottom TCO layer.^{15, 16} Then the source and drain electrodes (a-ITO), a- WO_3 active layer (100 nm), a-TaO_x electrolyte (250 nm), NiO counter layer (20 nm), and gate electrode (a-ITO) were deposited sequentially using stencil masks (**Fig. 2a**). The active channel size was 800 μm in length and 400 μm in width as schematically shown in **Fig. 2b**. The ITO, WO_3 and TaO_x films were amorphous, whereas the ZnO and NiO films were polycrystalline (**Fig. 3**).

Since a thin ZnO layer was inserted as a thin TCO, the electrical resistance switching ON/OFF ratio should be lower than previously reported ECTs without the bottom TCO layer (ON/OFF ratio $\sim 10^6$, **Fig. 1b**). The ON/OFF ratio can be controlled using the following equation, which describes the relationship between t_{WO_3} and t_{TCO} : $\log(ON/OFF) = \log(t_{WO_3}/t_{TCO}) + \log(\sigma_{WO_3}/\sigma_{TCO})$. **Figure 2c** shows the calculated ON/OFF ratio as a function of the thickness ratio of t_{WO_3} / t_{TCO} . Since a 30-nm-thick ZnO ($\sim 50 \text{ S cm}^{-1}$) was used, the maximum ON/OFF ratio was calculated be ~ 50 (red filled

circle).

4.3. Result and discussion

The TCO layer significantly improved the operation speed of the present ECT. **Figure 4a** shows the change in the sheet resistance (R_s) of the present ECT (w/ TCO) as a function of time during both the protonation ($V_g = +3$ V, left) and deprotonation ($V_g = -3$ V, right) stages at room temperature. The R_s of the ECT without the TCO layer is also shown for comparison (dotted line). When $V_g = +3$ V was applied, the R_s of the present ECT dropped from $\sim 3000 \Omega \text{ sq}^{-1}$ to $\sim 100 \Omega \text{ sq}^{-1}$ within 1 s. The ON/OFF ratio was ~ 30 , which is similar to the maximum ON/OFF ratio as described above. On the other hand, the ECT w/o TCO showed very slow decay of R_s ; the R_s changed slowly, taking >50 s from $\sim 10^7 \Omega \text{ sq}^{-1}$ to $\sim 90 \Omega \text{ sq}^{-1}$. In the case of deprotonation stages, the present ECT showed fast recovery of R_s within 1 s, and the operation of the present ECT device obeys Faraday's laws of electrolysis (see **Fig. 5**). These results clearly indicate that the present ECT with TCO layer can operated at much faster speed as compared to the previous ECT without the TCO layer.

The optical transmission changes in the present ECT are shown in **Figure 4b**. The transmission (T) of the deprotonation state was 67 % at the wavelength (λ) of 550 nm and has a high overall transmittance in the visible region. After a gate voltage application of + 3V, the transmittance dramatically decreased to 28 % at $\lambda = 550$ nm, and the average transmittance in the visible region was greatly reduced. To check the cyclability of the

4. Fast operation of a WO_3 -based solid-state electrochromic transistor

present ECT, alternating $V_g = \pm 3$ V at 4 s period was applied (i.e. 2 s at +3 V and 2 s at -3 V), and the sheet resistance was monitored (Fig. 6). Cyclability over 90 % was achieved after 500 repetitions, which ensures the good reversibility of the present ECT device.

Figure 7 shows a comparison between other WO_3 -ECTs and the present ECT in this work. The red star symbol represents the present ECT (operating voltage ± 3 V, and operating time 1 s) while the other WO_3 -ECTs with an asymmetric electrode configuration and liquid electrolyte are shown as blue circles. Although all-solid WO_3 -ECTs improve the operating time and voltage (shows the green symbol)^{3, 13, 17}, the operating speed was still slow as compared with WO_3 -ECTs using liquid electrolyte^{2, 7-10, 18, 19}. However, the present ECT can operate at voltages as low as 3 V and has a very fast operation time (less than 1 s). By inserting bottom TCO layer, a three terminal thin film transistor structure with parallel plate electrode configuration was realized. It is also worth noting that present device is all-solid state and free of liquid-electrolytes.

4.4. Conclusion

In summary, the all-solid high-speed and low-voltage operating ECT was achieved by inserting a TCO layer on the glass substrate. The operation speed of the present ECT at ± 3 V was less than 1 s, which is remarkably faster compared to the previously reported ECTs. Since all fabrication processes are performed at room temperature, the present ECT can be fabricated not only on glass substrates but also on flexible substrates such as plastics, which will have significant economic advantages. This new EC device structure will be advance the EC technology and advanced memory devices.

References

- [1] H. Akinaga and H. Shima, *Proc. IEEE* **98**, 2237-2251 (2010).
- [2] P. Barquinha, S. Pereira, L. Pereira, P. Wojcik, P. Grey, R. Martins and E. Fortunato, *Adv. Electron. Mater.* **1** (2015).
- [3] T. Katase, T. Onozato, M. Hirono, T. Mizuno and H. Ohta, *Sci. Rep.* **6**, 25819 (2016).
- [4] D. Y. Tu, D. Nilsson and R. Forchheimer, *J. Disp. Technol.* **9**, 755-759 (2013).
- [5] Z. Li, Y. Zhang, A. L. Holt, B. P. Kolasa, J. G. Wehner, A. Hampp, G. C. Bazan, T.-Q. Nguyen and D. E. Morse, *New J. Chem.* **35** (2011).
- [6] V. Jain, H. M. Yochum, R. Montazami and J. R. Heflin, *Appl. Phys. Lett.* **92** (2008).
- [7] M. Wang, S. Shen, J. Ni, N. Lu, Z. Li, H. B. Li, S. Yang, T. Chen, J. Guo, Y. Wang, H. Xiang and P. Yu, *Adv. Mater.* **29** (2017).
- [8] S. G. Altendorf, J. Jeong, D. Passarello, N. B. Aetukuri, M. G. Samant and S. S. Parkin, *Adv. Mater.* **28**, 5284-5292 (2016).
- [9] X. Leng, J. Pereiro, J. Strle, G. Dubuis, A. T. Bollinger, A. Gozar, J. Wu, N. Litombe, C. Panagopoulos, D. Pavuna and I. Bozovic, *npj Quantum Mater* **2** (2017).
- [10] C. ViolBarbosa, J. Karel, J. Kiss, O. D. Gordan, S. G. Altendorf, Y. Utsumi, M. G. Samant, Y. H. Wu, K. D. Tsuei, C. Felser and S. S. Parkin, *Proc. Nat.l Acad. Sci. U. S. A* **113**, 11148-11151 (2016).
- [11] J. T. Yang, C. Ge, J. Y. Du, H. Y. Huang, M. He, C. Wang, H. B. Lu, G. Z. Yang and K. J. Jin, *Adv. Mater.*, e1801548 (2018).
- [12] T. Tsuchiya, M. Jayabalan, K. Kawamura, M. Takayanagi, T. Higuchi, R. Jayavel and K. Terabe, *Jpn. J. Appl. Phys.* **57** (2018).
- [13] P. Grey, L. Pereira, S. Pereira, P. Barquinha, I. Cunha, R. Martins and E. Fortunato, *Adv. Electron. Mater.* **2** (2016).
- [14] T. Niwa and O. Takai, *Thin Solid Films* **518**, 1722-1727 (2010).
- [15] T. Minami, H. Nanto and S. Takata, *Appl. Phys. Lett.* **41**, 958-960 (1982).
- [16] R. E. I. Schropp and A. Madan, *J. Appl. Phys.* **66**, 2027-2031 (1989).
- [17] S. Thakoor, A. Moopenn, T. Daud and A. P. Thakoor, *J. Appl. Phys.* **67**, 3132-3135 (1990).
- [18] X. Meng, F. Quenneville, F. Venne, E. Di Mauro, D. Işık, M. Barbosa, Y. Drolet, M. M. Natile, D. Rochefort, F. Soavi and C. Santato, *J. Phys. Chem. C* **119**, 21732-21738 (2015).

4. Fast operation of a WO₃-based solid-state electrochromic transistor

[19] H. Kalhori, M. Coey, I. Abdolhosseini Sarsari, K. Borisov, S. B. Porter, G. Atcheson, M. Ranjbar, H. Salamati and P. Stamenov, *Sci. Rep.* **7**, 12253 (2017).

4. Fast operation of a WO_3 -based solid-state electrochromic transistor

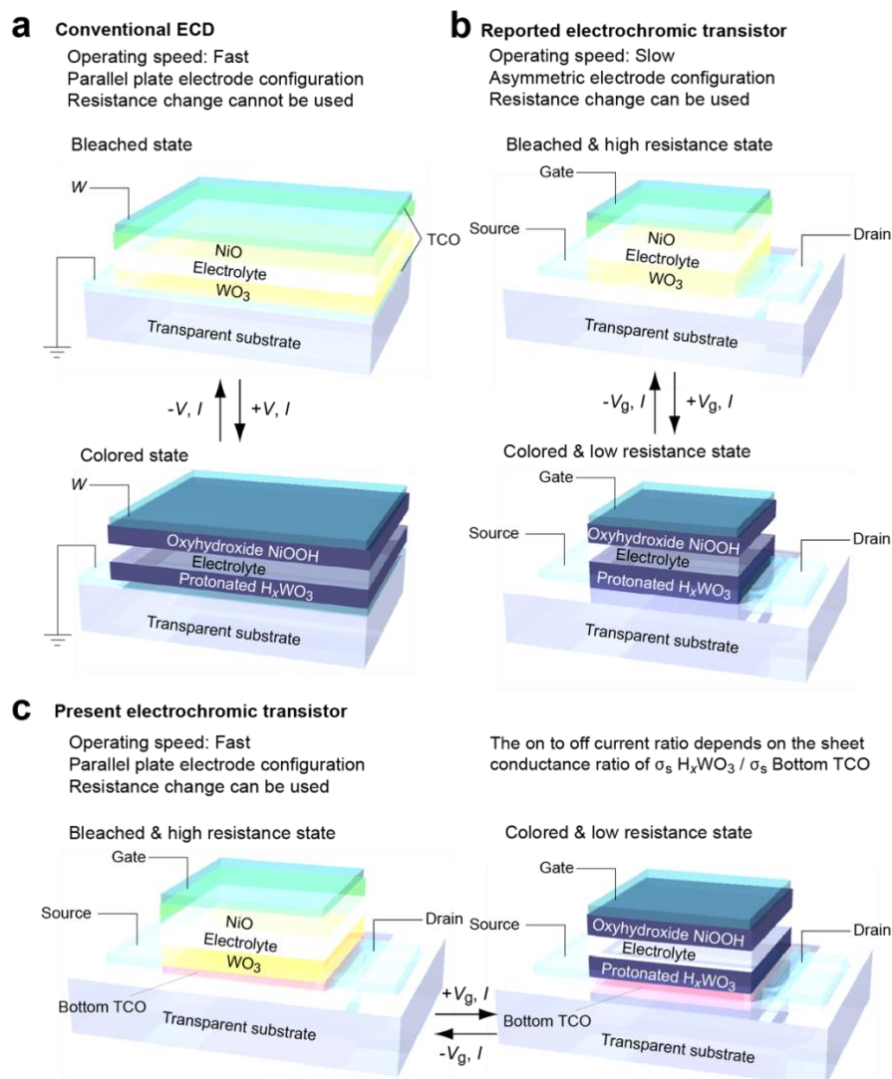


Figure 1. Electrochromic devices. Schematic device structures of (a) electrochromic displays (ECDs), (b) reported electrochromic transistor, and (c) present electrochromic transistor. All devices are composed of WO_3 , electrolyte, and NiO, which are sandwiched by two ITO (a transparent conducting oxide, ITO). Since there is a parallel plate electrode configuration, the operating speed of (a) is much faster than that of (b), of which the electrode configuration is asymmetric. Although one can use the resistance change in the case of (b), it cannot be used in the case of (a). In order to overcome this dilemma, the device structure (c) is proposed, which is a three terminal thin film transistor structure with parallel plate electrode configuration. It can be expected that the device (c) exhibits both fast transistor-like characteristic as well as the electrochromic display characteristics.

4. Fast operation of a WO_3 -based solid-state electrochromic transistor

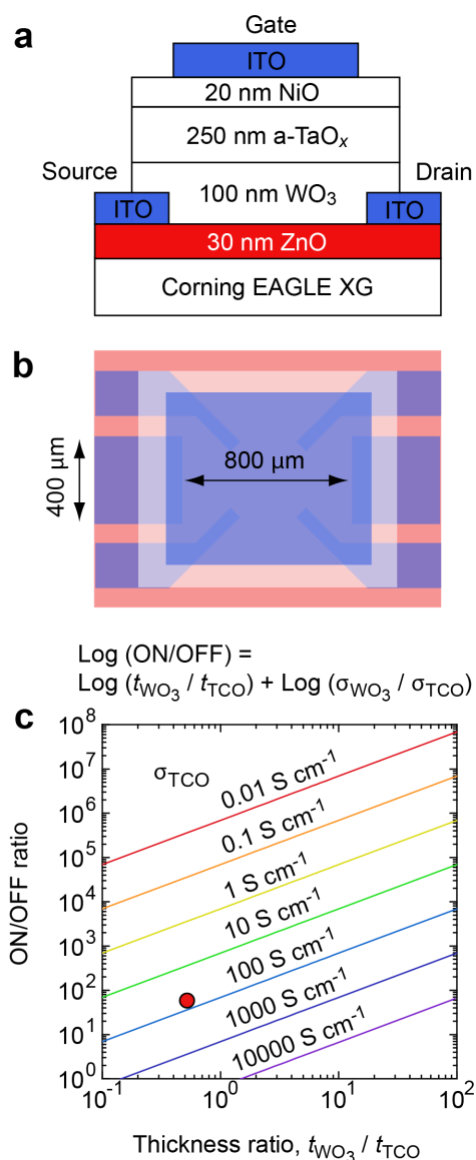


Figure 2. Present electrochromic transistor with the bottom TCO layer. (a) Schematic cross-sectional and (b) top view of the electrochromic transistor device. The device was fabricated on Corning EAGLE XG glass substrate. Using the stencil masks, ZnO was deposited as the bottom TCO layer (30 nm), ITO as the source and the drain electrodes, a-WO₃ layer (100 nm), solid-electrolyte a-TaO_x (250 nm) layer, and NiO layer. The active channel size is 800 μm in length and 400 μm in width. (c) It can be roughly hypothesized that the on-to-off current ratio depends on the thickness ratio of WO₃ and the TCO if the electrical conductivity of the TCO (σ) is fixed (the σ of HWO₃ was assumed to be 7000 S cm⁻¹). The red circle is showing the point of the present result.

4. Fast operation of a WO_3 -based solid-state electrochromic transistor

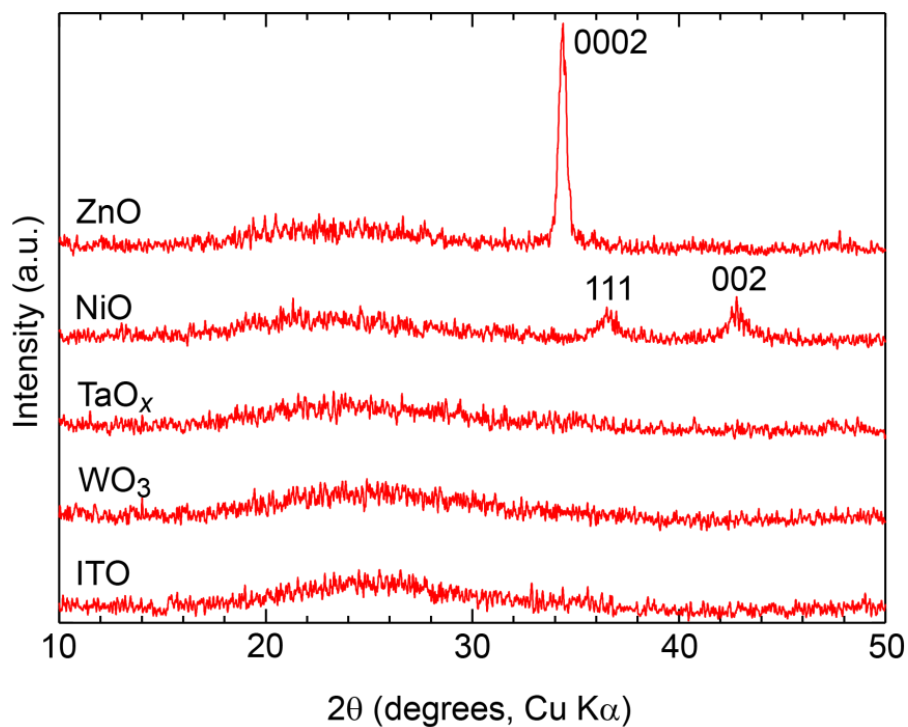


Figure 3. Glancing incidence XRD patterns of each layer of the present device. In the case of ZnO and NiO films, diffraction peaks of 0002 ZnO, and 111 and 002 NiO are seen, whereas only halo patterns are seen in TaO_x, WO₃, and ITO. These results clearly indicate that the TaO_x, WO₃, and ITO layers are amorphous, whereas ZnO and NiO are randomly oriented polycrystalline.

4. Fast operation of a WO_3 -based solid-state electrochromic transistor

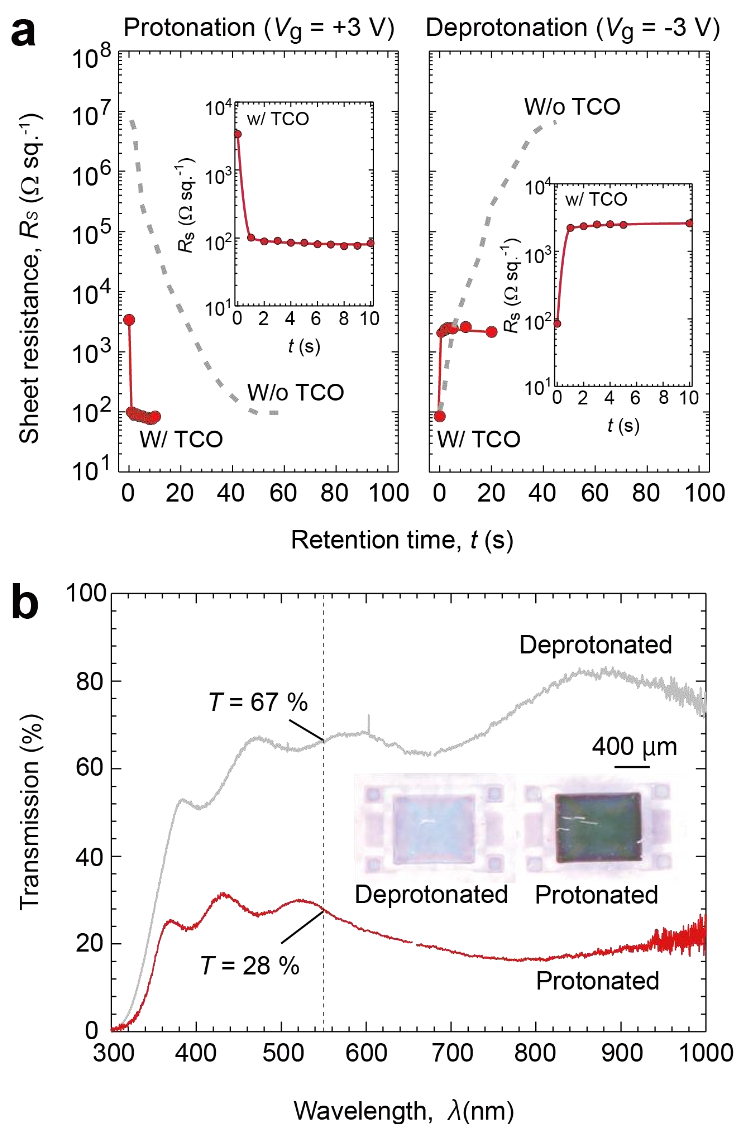


Figure 4. Change in the sheet resistance and the optical transmission before and after the protonation. (a) The decay of the sheet resistance (R_s) when +3 V is applied (left) and recovering of R_s when -3 V is applied. The result without the bottom TCO is also shown for comparison (dotted lines). The R_s drops within 1 s when +3 V is applied, whereas the R_s increases within 1 s when -3 V is applied. The operation time of the present device is much faster than the device without the TCO layer. (b) Optical transmission spectra of the present device. The transmission (T) of the deprotonated state (gray line) is 67 % at 550 nm whereas as the protonated state shows 28 % at $\lambda = 550$ nm. The inset shows the photographs of the device. After the protonation, the device becomes dark blue whereas the device was transparent at the deprotonated state.

4. Fast operation of a WO_3 -based solid-state electrochromic transistor

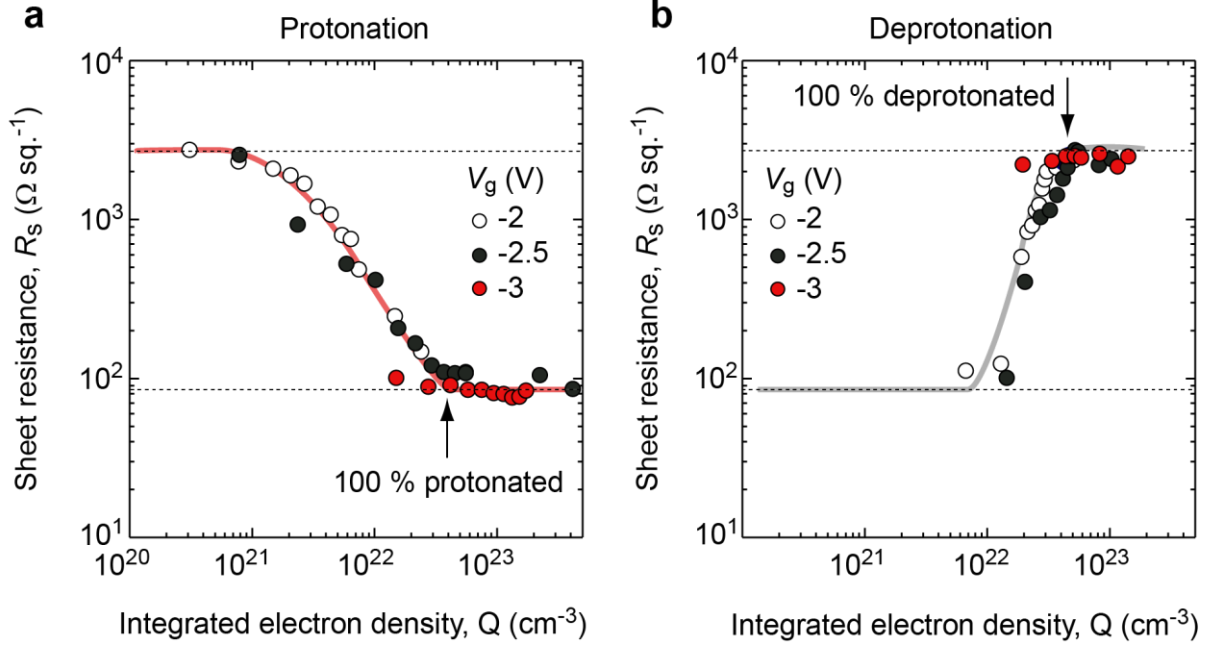


Figure 5. Sheet resistance of the device as a function of the integrated electron density (Q). Details of the calculation process of charge electron-density are described elsewhere. To achieve 100 % protonation/oxidation, $Q = 1.5 \times 10^{22} \text{ cm}^{-3}$ is required based on electrochromic reaction: $WO_3 + xH^+ + xe^- \rightarrow H_xWO_3$. The present ECT device obeys the Faraday's laws of electrolysis. (a) The R_s gradually decreases from $3 \times 10^3 \Omega \text{ sq.}^{-1}$ to $8 \times 10^1 \Omega \text{ sq.}^{-1}$ with increasing Q and saturates when Q is $4 \times 10^{22} \text{ cm}^{-3}$. (b) The R_s increases from $8 \times 10^1 \Omega \text{ sq.}^{-1}$ to $3 \times 10^3 \Omega \text{ sq.}^{-1}$ with increasing Q and saturates when Q is $4 \times 10^{22} \text{ cm}^{-3}$.

4. Fast operation of a WO_3 -based solid-state electrochromic transistor

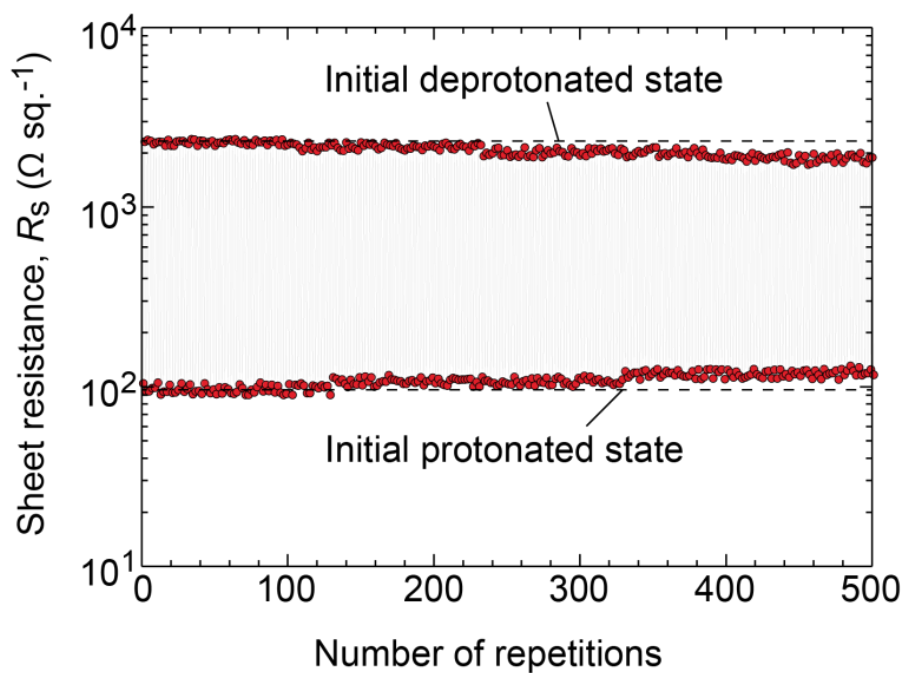


Figure 6. Cycle characteristics of the electrochromic transistor device. Repetitive property of the electrochromic device by applying repeatedly at $V_g = \pm 3$ V for 2 seconds. After 500 repetitions, the cyclability is more than 90 %.

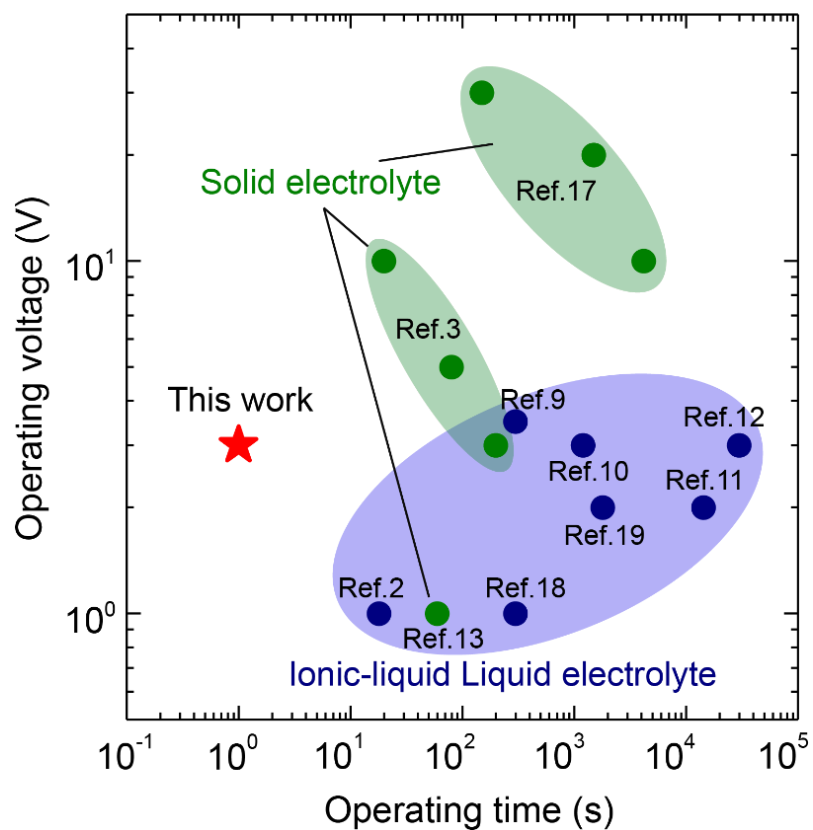


Figure 7. The operating voltage vs. the operating time. The operating time and voltage of the present device is 3 V and less than 1 s, which are smaller than that of the reported solid electrolyte devices (green) and ionic liquid or liquid electrolyte (blue) devices.

5. An oxide-based flexible electrochromic transistor under mechanical stress

5.1. Introduction

Mechanical flexibility has become an important feature for electronic devices as the elimination of mechanical constraints is essential for various applications including modern flat display panels (FPDs), solar cells, and sensors. Therefore, flexible electronics research area is rapidly growing¹. Experimentally demonstrated examples include: flexible-circuits², thin film transistors (TFTs)³, organic light emitting diodes (OLEDs)⁴, tensor sensors⁵, and solar cells^{6,7}. This chapter is devoted to adding flexibility in electrochromic transistors (ECTs), which can be utilized to simultaneously store both optical and electronic states^{8,9}.

Like TFTs, ECTs are composed of three electrodes of source, drain, and gate. However, their operation mechanism is different from that of conventional TFTs. In order to turn on/off the ECT, electrochemical redox reaction is utilized whereas pure electrostatic charge accumulation/depletion is utilized in TFTs. Similar to an electrochromic display (ECD)¹⁰⁻¹², the color of ECT can be modulated simultaneously with increase/decrease of the electrical resistivity. This is due to the changes in the valence state of the transition metal ion in the active material, which can be changed by the electrochemical redox reaction. Since the electrochemical redox reaction switches the chemical composition of the active material, ECTs can function as a non-volatile memory. In addition, the energy consumption is significantly low as compared to other FPDs such

5. An oxide-based flexible electrochromic transistor under mechanical stress

as liquid crystal displays (LCDs) and OLEDs.

ECT (ECD) is composed of electrolyte/active laminations of electrochromic material sandwiched by two electrodes. Previously, liquid electrolytes¹³⁻¹⁵ were used as the electrolyte of ECT. Therefore, previous ECTs were highly vulnerable to mechanical failures that can be caused by bending. In order to overcome this problem, recent studies successfully demonstrated the operation of all-solid-state ECTs^{9, 16-18}, which were fabricated at room temperature. Although the room temperature fabrication is compatible with economically viable flexible materials, all-solid-state ECTs on flexible substrates have not been demonstrated yet.

The all-solid-state ECT device consists of four different oxide layers including electrochromic amorphous WO_3 , water moisture containing TaO_x as porous gate insulator, shunting ZnO layer, and transparent conducting ITO electrodes.¹⁶ The mechanical properties of oxides tend to be brittle. Therefore, if these materials are deposited on flexible substrates as a device, clarifying the effect of mechanical strains on the device performance is crucial for understanding the physical flexural limitations as well as improving the flexibility.

This chapter demonstrates the operation of all-solid-state ECTs on flexible substrates and investigate the effect of static/cyclic flexural strains on the device performance. The flexible ECT without any strain showed excellent performances including fast operation within 1 s at low operation voltage of ± 3 V just like ECTs on rigid substrates¹⁶. The device showed strong resistant to static strains. However, its performance was highly vulnerable to cyclic stresses, which is typical mechanical characteristic of oxides. This

work suggests that the present flexible ECT has a great potential for curved display panels, and the flexural strain test results will be of great value in understanding the flexural durability of layer structured devices consist of oxide films.

5.2. Experimental

The flexible ECT device was fabricated on 100- μm -thick polyethylene terephthalate (PET) substrate (Nakai Industrial Ltd., $20 \times 20 \times 0.1$ mm). Except for the substrate, the device fabrication is almost the same with chapter 4. The oxide thin films were deposited by pulsed laser deposition (PLD, KrF excimer laser) at room temperature with different stencil masks. Two differently sized devices were prepared. The channel length (L) \times channel width (W) of the ECT were $100 \mu\text{m} \times 200 \mu\text{m}$ and $800 \mu\text{m} \times 400 \mu\text{m}$, respectively. First, 30-nm-thick polycrystalline ZnO film was deposited on a PET film as the bottom TCO layer, which applies a uniform electric field in the active layer and increases the operating speed¹⁶. Then 60nm-thick ITO/ZnO films were deposited as transparent electrodes (source and drain). Next, 100-nm-thick amorphous WO₃ active layer¹⁹, 250-nm-thick tantalum oxide (TaO_x) solid-electrolyte layer²⁰, and 20-nm-thick polycrystalline NiO layer were deposited sequentially on the bottom TCO layer. The NiO plays as a counter layer ($\text{NiO} + \text{OH}^- \rightarrow \text{NiOOH} + e^-$)²¹. Finally, 60-nm-thick ITO/ZnO bilayer film was deposited as the transparent gate electrode on the NiO layer. **Figure 1** shows the optical micrograph and schematic cross-sectional view of the resultant flexible ECT, which was bendable.

5.3. Result

Optical transmission

In order to check the electrochromism of the resultant flexible ECT, the optical transmission spectra were measured by UV-VIS Fiber-microscope (Source: L7893, HAMAMATSU Co., Detector: HR4000 High-Resolution Spectrometer, Ocean Optics Inc.). For protonation, a gate voltage (V_g) of +3 V was applied for 3 s to the flexible ECT. The as-prepared ECT was almost colorless and transparent, but it changed to dark blue upon protonation, which is similar to my previously reported ECT on rigid substrates.¹⁶ The optical transmission in the visible light region (400–800 nm in wavelength) drastically decreased to 28 % after protonation. However, upon de-protonation ($V_g = -3$ V for 3 s), the transmission recovered to 71 % in the visible region as shown in **Fig. 2**. The inset shows the optical micrograph of the protonated and de-protonated device, which clearly demonstrates the electrochromism of the resultant flexible ECT.

Effect of static flexural strain

Then the effect of bending on the electron transport of the ECT was examined during protonation and de-protonation using $800\ \mu\text{m} \times 400\ \mu\text{m}$ sized devices. The resultant ECT was bent at fixed radii of curvature (30 mm, 16 mm, 12 mm, and 6 mm) and protonation / de-protonation was performed in the device. **Figure 3(a)** shows the optical micrograph of the experimental setups of the bending test of the ECT devices at various radii of curvature. The tensile strain on the films was estimated with the ratio between half the

5. An oxide-based flexible electrochromic transistor under mechanical stress

substrate thickness and the radius of curvature (r)²², which yields 0.16 % for 30 mm, 0.31 % for 16 mm, 0.41 % for 12 mm, and 0.83 % for 6 mm. **Figure 3(b)** shows the sheet conductance (σ_s) as a function of operating gate voltage $\pm V_g$ at each radius of curvature. First, a positive gate voltage (V_g) from +0.5 V to +5 V was applied to protonate the device (**Fig. 3b** left panel, V_g application time of 1 s each), and then negative V_g also applied from -0.5 V to -5 V to de-protonate the device (**Fig. 3b** right panel, V_g application time of 1 s each). The σ_s values were measured by the dc four-probe method with van der Pauw electrode configuration with a source measure unit (Keithley 2450)^{9, 16}. The initial σ_s ($\sim 10^{-4} \Omega^{-1} \text{ sq}$) reflects the σ_s of the 30 nm ZnO thin film (bottom TCO layer). In case of curvature radius (r) = flat, 12 mm and 16 mm, the σ_s gradually increase then suddenly reach to $\sim 10^{-2} \Omega^{-1} \text{ sq}$ at +3 V. On the other hand, in case of $r = 12$ mm and 6 mm, $V_g = +3.5$ V and 4 V were required for σ_s to reach $\sim 10^{-2} \Omega^{-1} \text{ sq}$, respectively. Subsequently, by applying negative V_g , σ_s clearly recovered, reaching the initial state at $V_g = -3.5$ V. **Figure 3(c)** summarizes the retention-time (t) dependence of the R_s at various radii of curvature. The sheet resistance (R_s) was measured every 1 s after the protonation / de-protonation at room temperature. For protonation, positive d.c. gate voltage (+3 V) was applied to the ECT for 1 s, and then the R_s was measured. This sequence was repeated several times. Similarly, for de-protonation, negative d.c. gate voltage (-3 V) was applied to the ECT for 1 s, and then R_s was measured. This sequence was repeated several times as well. The solid lines are the results of the logistic function fitting. When r was larger than 16 mm, the relationship between R_s and retention time (t) did not change significantly; the R_s decreased from $\sim 4000 \Omega \text{ sq}^{-1}$ to $\sim 100 \Omega \text{ sq}^{-1}$ within 1 s during protonation and increased

5. An oxide-based flexible electrochromic transistor under mechanical stress

from $\sim 100 \Omega \text{ sq}^{-1}$ to $\sim 4000 \Omega \text{ sq}^{-1}$ within 1 s during de-protonation. However, R_s started to increase when the r was below 16 mm, and the operating time increased slightly from < 1 s to 2–3 s.

Overall, flexural strains increased the operation voltage and operation time of the flexible ECTs, and the protonation stages were affected a bit more strongly. Surprisingly, despite the changes in the operation time, the absolute values of R_s after protonation/deprotonation were not significantly affected by the static flexural strains. This suggests that the active WO_3 and shunting ZnO remain unharmed up to $r = 6$ mm. On the other hand, the resistance of the top gate electrode before the bending experiment was $\sim 100 \Omega$, but it increased to $\sim 10 \text{ k}\Omega$, after the bending test at radius $r = 6$ mm. This indicates the operation delay due to the flexural strains is mainly attributed to mechanical damages in the ITO/ ZnO electrodes (gate). This is likely attributed to the fact that the outermost layer is under the highest tensile strain. Therefore, the static flexure strain degrades the operation speed, but overall, the present flexible ECTs show great performance which 3V, 1sec operation in $r > 16$ mm. These results indicate that present ECTs are resistant to static flexural strains and have the potential for curved display applications.

Effect of dynamic flexural strain

Finally, the effect of cyclic flexural strains on the flexible ECT device performance was investigated. Bending moments (i.e. minimum strain = 0, maximum strain $\neq 0$) were repeatedly exerted to the flexible ECTs, and the bending axis was parallel to the long axis

5. An oxide-based flexible electrochromic transistor under mechanical stress

of the device. $800\ \mu\text{m} \times 400\ \mu\text{m}$ sized device worked only for 50 flexural cycles even under at $r = 16\ \text{mm}$. Since resistance to cracking increases with decreasing size, the cyclic tests were performed using $200\ \mu\text{m} \times 100\ \mu\text{m}$ sized device. The ECT was bent 10 times, then performed protonation / de-protonation. After each protonation / de-protonation, the two-terminal resistance was measured. Since the $200\ \mu\text{m} \times 100\ \mu\text{m}$ size device only has a two-terminal source-drain electrode, two-terminal resistance (R) and sheet resistance (R_s) can be compared by $R_s = R(W/L)$. The test was performed until the device showed infinite resistance, which indicates a complete mechanical failure in the device (or fatigue limit). **Figure 4** shows the changes in the two-terminal resistance ($R_{\text{deprotonation}}$, $R_{\text{protonation}}$) as a function of flexural cycles at various r ($r = 16, 12$ and $6\ \text{mm}$). At $r = 16, 12$, and $6\ \text{mm}$, the device lasted $\sim 410, \sim 220$, and ~ 30 cycles, respectively. Before the test, the ECT showed $R_{\text{deprotonation}} \sim 35\ \text{k}\Omega$ and $R_{\text{protonation}} \sim 1\ \text{k}\Omega$. Both $R_{\text{deprotonation}}$ and $R_{\text{protonation}}$ gradually increased with the number of cycles.

5.4. Discussion

In general, cyclic flexural strains have a significant effect on the device compared to static flexural strains. During the cyclic flexural strains test, the resistance values of the active WO_3 layer and ZnO layer, which are directly related to protonated and de-protonated states, gradually increased in all cases. This suggests that both the active WO_3 and shunting ZnO are being affected by the cyclic flexural strains, which is drastically different from the effect of static flexural strains. This is not surprising since most materials show higher strengths in static strain tests²³. These results show that the present

5. An oxide-based flexible electrochromic transistor under mechanical stress

ECTs are highly susceptible to fatigue and not suitable for applications that require dynamic strain resistant unless the radius of curvature is large.

Furthermore, the optical micrographs of the device were obtained after bending tests by Laser scanning microscope (VK-9710, KEYENCE). The optical micrographs of the fractured devices at their fatigue limits after cyclic flexural strains are shown in Fig. 5(a), (b), and (c), the radii is $r = 16, 12$ and 6 mm, respectively. At all radii, the cracks in the device resemble mode I fracture, where the crack propagation direction and the fracture surface are perpendicular to the tensile stress. Above $r = 12$ mm, a series of straight crack lines are observed, which are typical brittle fracture characteristics commonly observed from amorphous oxide films²⁴⁻²⁷. This strongly suggests that the crack initiates in the outer ITO top gate electrode, which is consistent with the device performance tests. However, at $r = 6$ mm, the long crack lines become short elliptical pores that are clustered. This suggests a change in the fracture mechanism when r decreases from 12 mm to 6 mm. The new failure mechanism is likely attributed to the fracture of porous TaO_x since short elliptical pores come from the evolution of micropores²³. This cracking mechanism is likely related to the sharp performance degradation during the cyclic flexural stress tests at $r = 6$ mm as well as the large device ($800 \mu\text{m} \times 400 \mu\text{m}$, only lasted 50 cycles) since these cracks are initiated at the micropores and the $200 \mu\text{m} \times 100 \mu\text{m}$ sized device exhibits less number of pores. Compared to failures in ITO, mechanical damages in TaO_x is much more critical to the device performance since the active WO₃ is directly in contact with

5. An oxide-based flexible electrochromic transistor under mechanical stress

the TaO_x. The fracture characteristics demonstrate that the flexure strengths of ETCs are limited by the ITO electrode and TaO_x at low and high tensile strains, respectively.

The present flexible ETCs exhibited good resistance to static flexural strains, and the corresponding performance degradation is a minor delay in the device operation with no damages in the WO₃ and ZnO layers. Since the main damage in the device structure is in the ITO/ZnO electrodes, changing the gate electrode to flexible materials²⁸ or fabricating special structure²⁹⁻³² would improve the device performance under static flexural strains. In contrast, fatigue from cyclic flexural strains noticeably degraded the electrical properties of WO₃ and ZnO, which decreased the ECT performance. The fatigue limit drastically decreases if r changes from 12 mm to 6 mm, and $r > 16$ mm seems to be necessary to maintain reasonable device performance under cyclic flexure stresses. Adding another layer that exerts compressive strains on the device can potentially negate the tensile strains from bending, but detailed failure analysis in the future is necessary to improve the cyclic flexural durability of the present device.

5.5. Conclusion

In summary, this chapter demonstrated the performance of a flexible ETC on 0.1-mm-thick polyethylene terephthalate substrate, which was fabricated using pulsed laser deposition technique at room temperature. The ETC consists of electrochromic tungsten oxide, water containing porous gate insulator tantalum oxide, and transparent conducting ITO. The resultant ETCs showed fast operation within 1 s at low operation voltage of ± 3

5. An oxide-based flexible electrochromic transistor under mechanical stress

V while showing excellent resistance to static flexural strains. However, their performances were strongly degraded by cyclic flexural stresses and fatigues, which were evident from the crack formations in the device. Therefore, high bending radius ($r > 16$ mm) is required for sustaining acceptable device characteristics. Since the present flexible ECT can be fabricated at room temperature, low cost polymer-based substrates can be used. The strong resistance to static flexural strains observed from the present ECTs would be of great value for economically viable curved FPD devices in the future.

References

- [1] M. Kaltenbrunner, T. Sekitani, J. Reeder, T. Yokota, K. Kuribara, T. Tokuhara, M. Drack, R. Schwodiauer, I. Graz, S. Bauer-Gogonea, S. Bauer and T. Someya, *Nature* **499**, 458-463 (2013).
- [2] T. Sekitani, U. Zschieschang, H. Klauk and T. Someya, *Nat Mater* **9**, 1015-1022 (2010).
- [3] K. Nomura, H. Ohta, A. Takagi, T. Kamiya, M. Hirano and H. Hosono, *Nature* **432**, 488-492 (2004).
- [4] T. Yokota, P. Zalar, M. Kaltenbrunner, H. Jinno, N. Matsuhisa, H. Kitanosako, Y. Tachibana, W. Yukita, M. Koizumi and T. Someya, *Sci. Adv.* **2**, 8 (2016).
- [5] S. Lee, A. Reuveny, J. Reeder, S. Lee, H. Jin, Q. Liu, T. Yokota, T. Sekitani, T. Isoyama, Y. Abe, Z. Suo and T. Someya, *Nat Nanotechnol* **11**, 472-478 (2016).
- [6] H. Kimura, K. Fukuda, H. Jinno, S. Park, M. Saito, I. Osaka, K. Takimiya, S. Umezu and T. Someya, *Adv. Mater.* **31**, e1808033 (2019).
- [7] M. Kaltenbrunner, M. S. White, E. D. Glowacki, T. Sekitani, T. Someya, N. S. Sariciftci and S. Bauer, *Nat Commun* **3**, 770 (2012).
- [8] P. Barquinha, S. Pereira, L. Pereira, P. Wojcik, P. Grey, R. Martins and E. Fortunato, *Adv. Electron. Mater.* **1** (2015).
- [9] T. Katase, T. Onozato, M. Hirono, T. Mizuno and H. Ohta, *Sci. Rep.* **6**, 25819 (2016).
- [10] S. K. Deb, *Sol. Energy Mater. Sol. Cells* **92**, 245-258 (2008).
- [11] V. Jain, H. M. Yochum, R. Montazami and J. R. Heflin, *Appl. Phys. Lett.* **92** (2008).
- [12] T. Niwa and O. Takai, *Thin Solid Films* **518**, 1722-1727 (2010).
- [13] S. G. Altendorf, J. Jeong, D. Passarello, N. B. Aetukuri, M. G. Samant and S. S. Parkin, *Adv. Mater.* **28**, 5284-5292 (2016).
- [14] M. Wang, S. Shen, J. Ni, N. Lu, Z. Li, H. B. Li, S. Yang, T. Chen, J. Guo, Y. Wang, H. Xiang and P. Yu, *Adv. Mater.* **29** (2017).
- [15] X. Meng, F. Quenneville, F. Venne, E. Di Mauro, D. Işık, M. Barbosa, Y. Drolet, M. M. Natile, D. Rochefort, F. Soavi and C. Santato, *J. Phys. Chem. C* **119**, 21732-21738 (2015).
- [16] T. Onozato, Y. Nezu, H. J. Cho and H. Ohta, *AIP Adv.* **9** (2019).
- [17] P. Grey, L. Pereira, S. Pereira, P. Barquinha, I. Cunha, R. Martins and E. Fortunato, *Adv. Electron. Mater.* **2** (2016).

5. An oxide-based flexible electrochromic transistor under mechanical stress

- [18] S. Thakoor, A. Moopenn, T. Daud and A. P. Thakoor, *J. Appl. Phys.* **67**, 3132-3135 (1990).
- [19] P. G. Dickens and M. S. Whittingham, *Quarterly Reviews, Chemical Society* **22**, 30-44 (1968).
- [20] M. J. Duggan, T. Saito and T. Niwa, *Solid State Ionics* **62**, 15-20 (1993).
- [21] X. H. Xia, J. P. Tu, J. Zhang, X. L. Wang, W. K. Zhang and H. Huang, *Sol. Energy Mater. Sol. Cells* **92**, 628-633 (2008).
- [22] L. Pereira, D. Gaspar, D. Guerin, A. Delattre, E. Fortunato and R. Martins, *Nanotechnology* **25**, 094007 (2014).
- [23] W. D. Callister and D. G. Rethwisch, *Fundamentals of Materials Science and Engineering*, 5 edition ed. (Wiley, London, 2015).
- [24] C. Peng, Z. Jia, H. Neilson, T. Li and J. Lou, *Adv. Eng. Mater.* **15**, 250-256 (2013).
- [25] J. L. Ni, X. F. Zhu, Z. L. Pei, J. Gong, C. Sun and G. P. Zhang, *J. Phys. D: Appl. Phys.* **42** (2009).
- [26] D. R. Cairns, R. P. Witte, D. K. Sparacin, S. M. Sachsman, D. C. Paine, G. P. Crawford and R. R. Newton, *Appl. Phys. Lett.* **76**, 1425-1427 (2000).
- [27] S. K. Park, J. I. Han, D. G. Moon and W. K. Kim, *Jpn. J. Appl. Phys.* **42**, 623-629 (2003).
- [28] D. Soo Choi, S. Ho Han, H. Kim, S. Hee Kang, Y. Kim, C. M. Yang, T. Y. Kim, D. Ho Yoon and W. Seok Yang, *Nanotechnology* **25**, 395702 (2014).
- [29] K. Sakamoto, H. Kuwae, N. Kobayashi, A. Nobori, S. Shoji and J. Mizuno, *Sci. Rep.* **8**, 2825 (2018).
- [30] J. Yun, Y. H. Park, T. S. Bae, S. Lee and G. H. Lee, *ACS Appl Mater Interfaces* **5**, 164-172 (2013).
- [31] S. J. Lee, Y. Kim, J. Y. Hwang, J. H. Lee, S. Jung, H. Park, S. Cho, S. Nahm, W. S. Yang, H. Kim and S. H. Han, *Sci. Rep.* **7**, 3131 (2017).
- [32] X. Zhang, X. Liu, Y. Zhang, R. Bao, D. Peng, T. Li, G. Gao, W. Guo and C. Pan, *J. Mater. Chem. C* **4**, 8130-8134 (2016).

5. An oxide-based flexible electrochromic transistor under mechanical stress

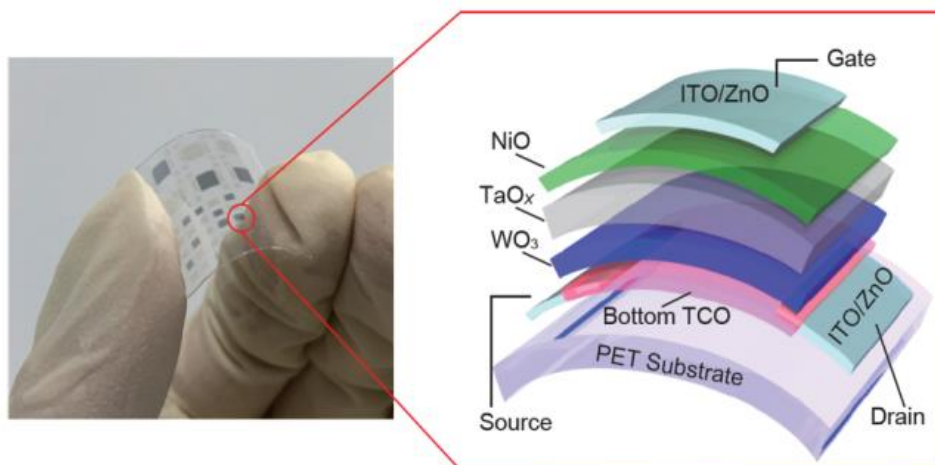


Figure 1. A flexible ECT. Using the stencil masks, the ECT was fabricated on 0.1-mm-thick PET substrate. The resultant ECT is bendable.

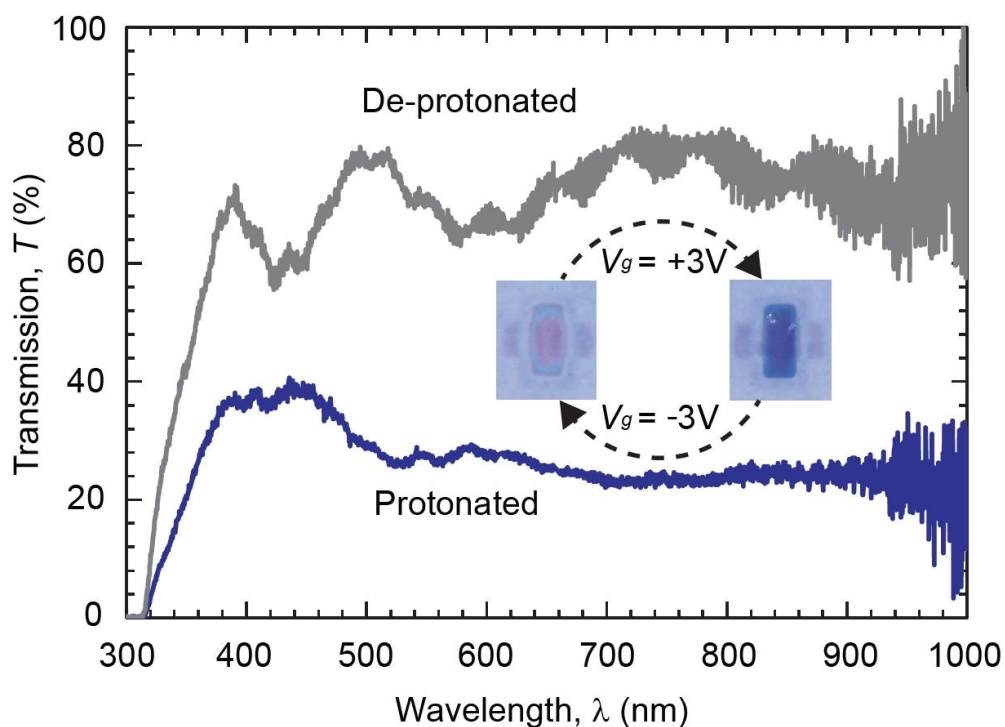


Figure 2. Optical transmission spectra of the flexible ECT, which is composed of 50-nm-thick ITO, 10-nm-thick ZnO, 20-nm-thick NiO, 250-nm-thick TaO_x, 100-nm-thick WO₃, 10-nm-thick ZnO, and 0.1-mm-thick PET. The optical transmission in the visible light region dramatically decreased after the protonation, and it recovered after the de-protonation. The inset shows the photographs of the device. After the protonation (applied $V_g = +3V$), the device becomes dark blue whereas the device was transparent at the de-protonation (applied $V_g = -3V$).

5. An oxide-based flexible electrochromic transistor under mechanical stress

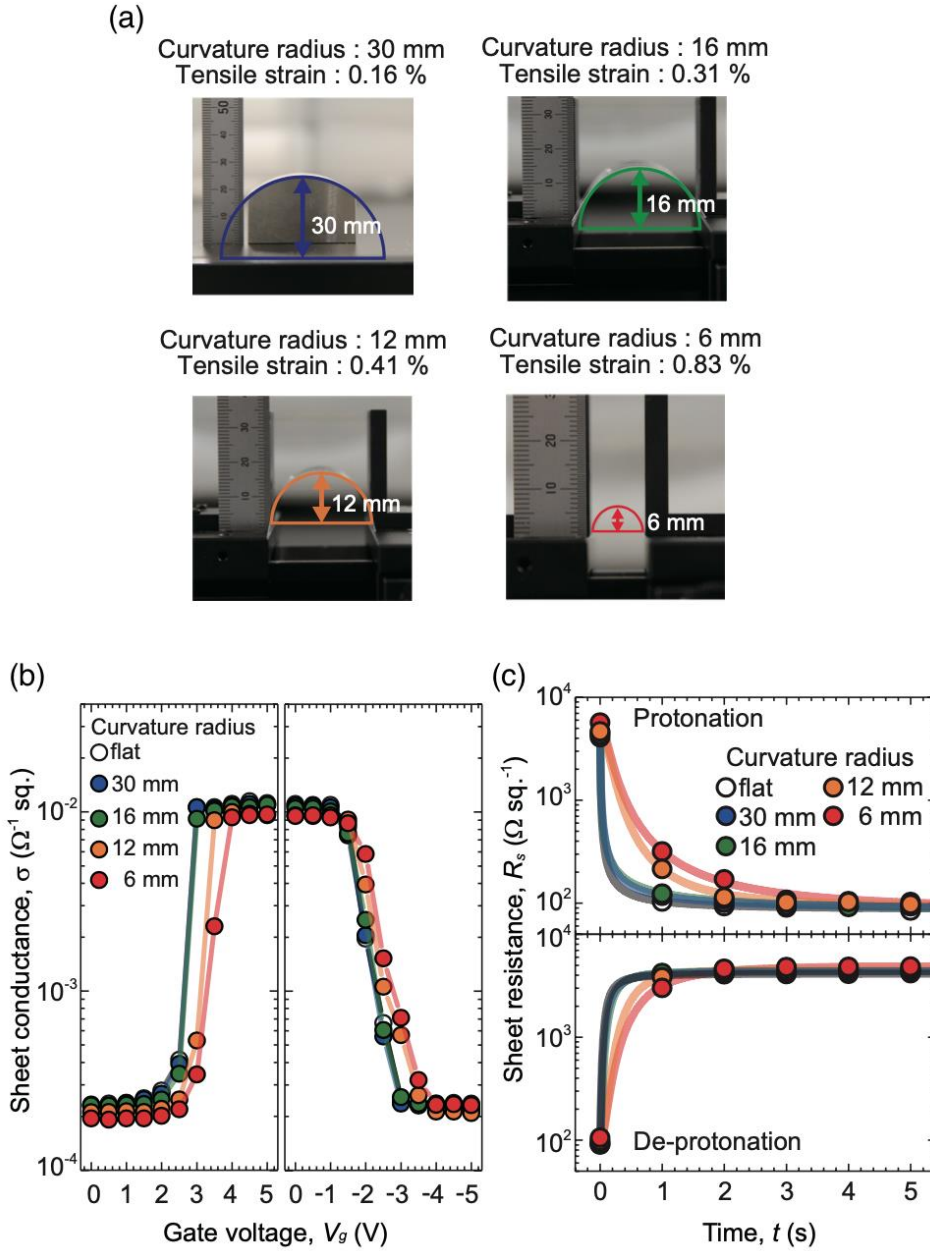


Figure 3. (a) The optical micrographs of the experimental setups of the bending test of the ECT devices at various radii of curvature. The tensile strain was kept at 0.16 % for 30 mm, 0.31 % for 16 mm, 0.41 % for 12 mm, and 0.83 % for 6 mm. (b) Sheet conductance (σ_s) as a function of applied Gate voltage (V_g) at various curvature radius, where positive V_g applied for protonation (left panel, V_g application time of 1s each), and then negative V_g applied for deprotonation (right panel, V_g application time of 1s each). (c) Effect of bending on the electron transport of the ECT during protonation and de-protonation. Retention time (t) dependence of sheet resistance (R_s) under application of $\pm V_g = 3$ V.

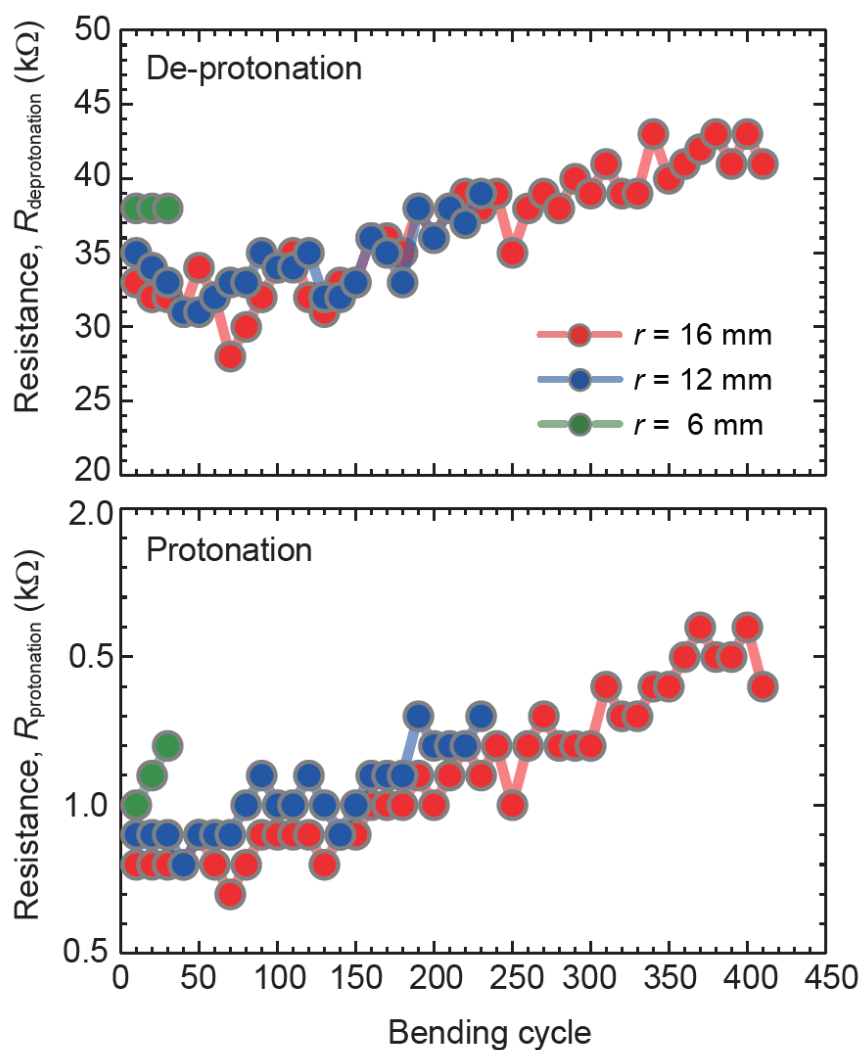


Figure 4. Change in the two-terminal resistance ($R_{\text{deprotonation}}$, $R_{\text{protonation}}$) as a function of flexural cycles at the various r ($r = 16, 12$ and 6 mm). The ECT showed reasonable device characteristics even after 410 cycles of the bending test ($r = 16$ mm).

5. An oxide-based flexible electrochromic transistor under mechanical stress

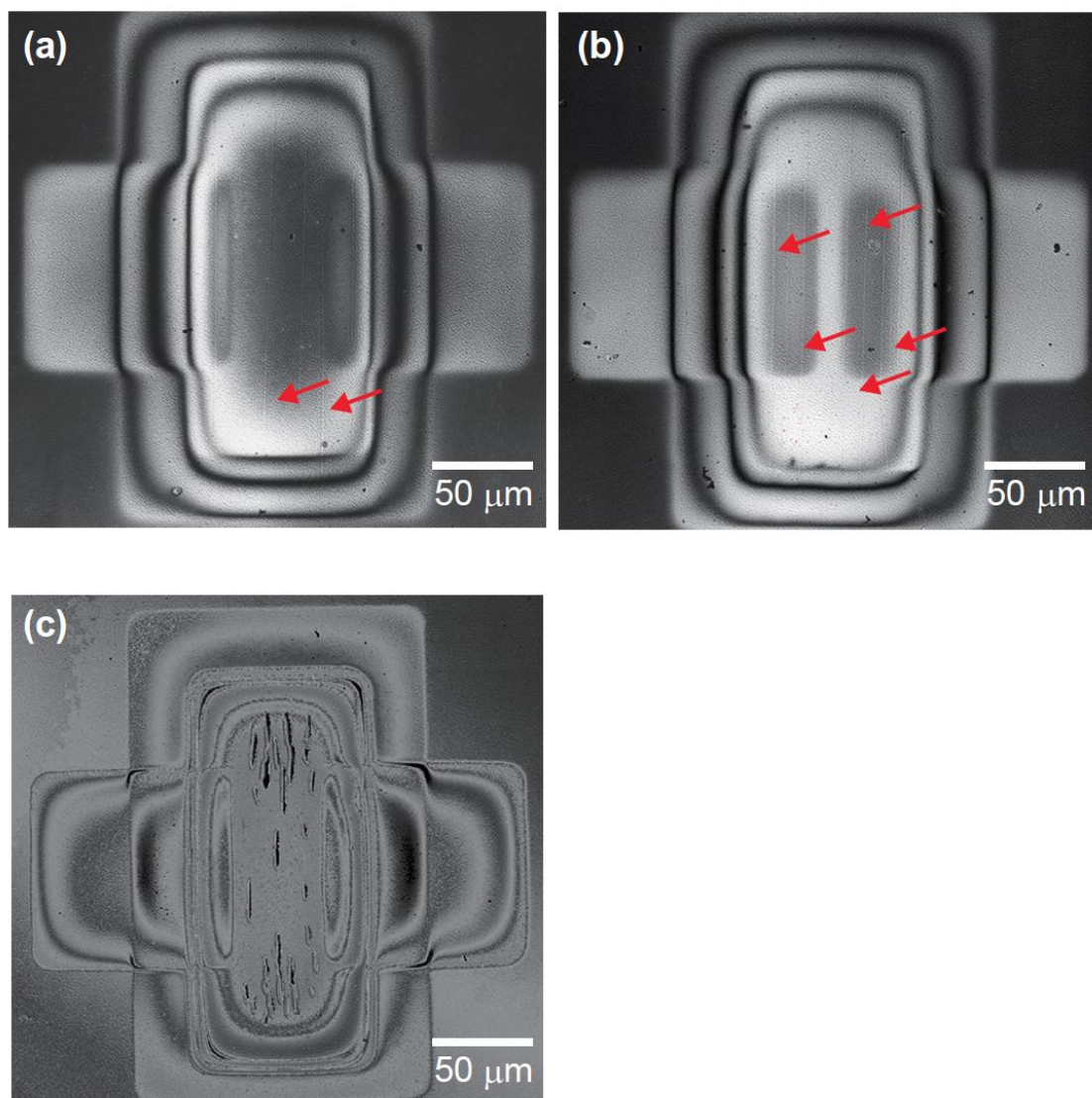


Figure 5. Optical micrographs of ECTs at their fatigue limits, obtained by a laser microscope. The radii of curvature are: (a) $r = 16$ mm, (b) $r = 12$ mm, and (c) $r = 6$ mm. Above, $r = 12$ mm, the crack lines are long and straight, which are typical brittle fracture characteristics of thin amorphous films. However, at $r = 6$ mm, clustered short elliptical pores are shown, which is likely from the fracture of porous TaO_x .

6. Summary

In this research, oxide-based electrochromic transistors (ECTs) was developed using an a-WO₃ thin film as the active layer, which exhibited the functionality of both the electrochromic displays (ECDs) and three-terminal transistors. Present WO₃-based ECTs have potential as multifunctional electronic devices because WO₃-based ECTs turn from highly resistive to conductive state when a positive gate voltage is applied. At the same time, the color of the ECT turns from almost colorless transparent to dark blue. Thus, it can exhibit display information and electrical resistance information simultaneously.

The chapter3 demonstrated all-solid a-WO₃ based electrochromic transistors. Tungsten trioxide (WO₃), a well-known electrochromic (EC) material for the smart window, is a wide bandgap insulator but becomes a metallic conductor H_xWO₃ upon protonation. Although the electrochromism can be utilized with metal-insulator (MI) switching in one device, such EC-MI switching could be utilized in previous EC devices because of their two-terminal structure with parallel-plate configuration. Here, a transparent EC-MI switchable device with a three-terminal TFT-type structure was demonstrated using an amorphous a-WO₃ channel layer, which was fabricated on a glass substrate at room temperature. Water-infiltrated nano-porous glass, CAN (calcium aluminate with nano-pores), was used as a liquid-leakage-free solid gate insulator. At the as-deposited state, the device was fully transparent in the visible-light region. Upon applying a positive gate voltage, the active channel became dark blue, and the electrical resistivity of the a-WO₃ layer drastically decreased due to protonation. Upon applying a

6. Summary

negative gate voltage, deprotonation occurred, and the active channel returned to a transparent insulator.

In the chapter4, a WO_3 -based electrochromic transistor with a fast operation speed was successfully developed. Although an all-solid oxide-based electrochromic transistor was demonstrated earlier, those devices had long operating speed (operating time ~ 20 s) and required high-operating voltage ($V_g = \sim 10$ V) due to their asymmetric gate-source electrode configuration. Here, a fast operation of a solid-state ECT was achieved. A solid-state ECT with three terminal gate-source-drain electrodes was fabricated using an amorphous WO_3 film as the electrochromic material and amorphous TaO_x as the solid electrolyte. With the insertion of a thin ZnO layer between the source and drain electrodes to achieve a pseudo symmetric gate-source electrode configuration, the operation time was greatly reduced to less than 1 s at the gate voltage of ± 3 V while keeping the on-to-off ratio of ~ 30 .

In the chapter5, since the oxide-based electrochromic transistor in this research can be fabricated at room temperature process, flexible substrates were used to fabricate flexible devices. This chapter focused on the device operation and mechanical endurance of a tungsten oxide-based flexible electrochromic transistor (ECT), which was fabricated on a 0.1-mm-thick polyethylene terephthalate film. The ECT can be operated by applying a voltage of ± 3 V for 1 s when the radius of curvature was larger than 16 mm, indicating that the flexible ECT exhibited strong resistance to static strains. However, the resistance of the channel increased by fatigues from applying cyclic flexural strains. Present flexible ECT would highly be useful for the economically viable curved display panels. However,

6. Summary

its vulnerability to fatigue needs improvements for other applications.

This research proposed and developed a three-terminal oxide-based ECT that can utilize the electrical and optical changes due to EC phenomena of transition metal oxides. Amorphous WO_3 was selected as the active layer, and the three-terminal transistor structure was adapted for utilizing both the electrical and optical changes of WO_3 . The fabrication and operation of all-solid ECT by using a solid electrolyte were successful. In addition, by inserting ZnO thin film as bottom TCO, the operating speed was improved (~ 20 s \rightarrow within 1 s). The ECTs fabricated on a flexible substrate can operate at high speed even in a bending state of $r > 16$ mm.

Table 1 summarizes and compares the characteristics of ECT, liquid crystal display (LCD), and flash memory. LCD is a typical information display device that utilizes color tone changes, which can operate within milliseconds but requires standby power due to its volatile nature. Thus, LCD does not work as an information storage device. Flash memory device can store information and has a very fast operation speed ($10^{-9} \sim 10^{-3}$ sec). Although the flash memory such as USB memory is widely used, it has can only utilize electrical resistivity changes and has only one-bit information capacity of 0 or 1. On the contrary, the ECTs developed in this research fulfill expectations for advanced multifunctional devices, which can utilize not only electrical resistance changes but also optical color changes.

Figure 1 shows an application example of electronic equipment using ECTs. Placing ECTs on the window and combining it with touch panel technology may enable the window to be used as a transparent-electronic blackboard. In addition, ECTs can be

6. Summary

placed on curved displays because it has flexibility. I envision that these ECTs technologies will move the technology of the electronic device forward and be utilized in advanced multifunctional devices.

6. Summary

	ECT	LCD	Flash memory
Operating speed	~1 sec	10^{-3} sec	$10^{-9} \sim 10^{-3}$ sec
Color change	○	○	×
Resistivity change	○	×	○
Non-volatile	○	×	○

Table 1. Summary and comparisons of the characteristics of ECT, LCD, and flash memory.

6. Summary

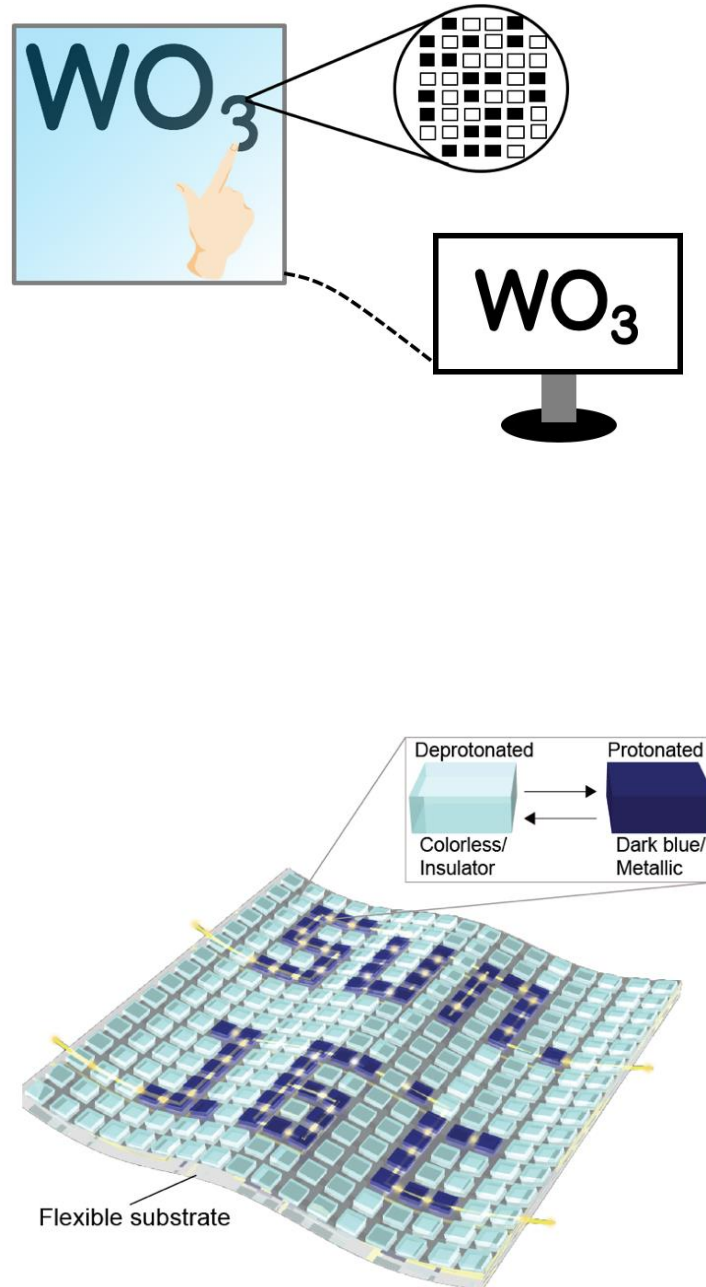


Figure 1. Application example of electronic equipment using ECTs. (upper) Placing ECT on the window and combining it with touch panel technology may enable the window to be used as a transparent-electronic blackboard. (bottom) The ECTs placed on the curved panel display.

Acknowledgments

The present study was conducted in Prof. Hiromichi Ohta Laboratory (Laboratory of Functional Thin Film Materials) at Research Institute for Electronic Science (RIES), Hokkaido University from April 2015 to March 2020, including master course.

First of all, I would like to express my deepest gratitude to Prof. Hiromichi Ohta, my supervisor, for his precise guidance and supports. In 2013, Prof. Ohta was given the chance to me to visit his laboratory as a summer Internship, which is an incredible experience for me. After entering his laboratory, he introduced me to the field of oxide materials and given me many opportunities. During the five years, he taught to me the basics attitude of a researcher, such as what research is. The knowledge of research and attitudes towards the life he taught me will always be helpful to me in the future.

I would also like to special thank Prof. Michihiko Yamanouchi (RIES, Hokkaido Univ.), Prof. Takayoshi Katase (Tokyo Institute of Technology) and Prof. Hai Jun Cho (RIES, Hokkaido Univ.). They provided me with many advice and precise guidance throughout this study. Without their helps and discussions, I cannot fulfil my recent research works.

I am deeply grateful to the members of Prof. Ohta's group. Prof. Anup Kumar Sanchela (Currently, Assistant Professor, Pandit Deendayal Petroleum University.), Dr. Yuqiao Zhang (PD, RIES, Hokkaido Univ.), Ms. Gowoon Kim (Ph.D candidate, IST, Hokkaido Univ.), Ms. Mian Wei (Ph.D candidate, IST, Hokkaido Univ.), Ms. Doudou Liang (Ph.D candidate, USTB), Ms. Qian Yang (Ph.D candidate, IST, Hokkaido Univ.),

Acknowledgments

Mr. Yuzhang Wu (Ph.D candidate, IST, Hokkaido Univ.), Mr. Kenyu Sugo(Master candidate, IST, Hokkaido Univ.), Mr. Koichi Sato (Master candidate, IST, Hokkaido Univ.), Mr. Yugo Takashima (Master candidate, IST, Hokkaido Univ.), Mr. Lizabeth Gong(Master candidate, IST, Hokkaido Univ.), et al. for the helps during my study and life in Prof. Ohta's Lab.

I am grateful to financial support during my study in the Ph.D. program by the Japan Society for the Promotion of Science (JSPS). Without the JSPS Research Fellowships for Young Scientists support would not have been possible for me to complete the Ph.D. program.

Finally, I would like to show my deepest appreciation to my parents Hirotohi & Yuko Onozato, my sister Mari Onozato and my all friends, who have given me a chance and great supports. Their supports have always been the driving force to my study and life in Hokkaido University these five years.

February 2020

Takaki Onozato

Publication lists

Papers related to this thesis

1. **Takaki Onozato**, Hai Jun Cho, and Hiromichi Ohta, “An oxide-based flexible electrochromic transistor under mechanical stress”, *Jpn. J. Appl. Phys.* **59**, 024002 (2020).
2. **Takaki Onozato**, Yukio Nezu, Hai Jun Cho, and Hiromichi Ohta, “Fast operation of a WO₃-based solid-state electrochromic transistor”, *AIP Advances* **9**, 025122 (2019).
3. T. Katase, **T. Onozato**, M. Hirono, T. Mizuno, and H. Ohta, “A transparent electrochromic metal-insulator switching device with three-terminal transistor geometry”, *Sci. Rep.* **6**, 25819 (2016).

Other papers

1. Hai Jun Cho, Yugo Takashima, Yukio Nezu, **Takaki Onozato**, and Hiromichi Ohta, “Anisotropic Heat Conduction in Ion Substituted Layered Cobalt Oxides”, *Adv. Mater. Interfaces* **7**, 1901816 (2019).
2. Hai Jun Cho, Bin Feng, **Takaki Onozato**, Mian Wei, Anup Sanchela, Yuichi Ikuhara, and Hiromichi Ohta, “Investigation of electrical and thermal property reductions in La-doped BaSnO₃ films”, *Phys. Rev. Materials* **3**, 094601 (2019).

3. Hai Jun Cho, Gowoon Kim, **Takaki Onozato**, Hyoungjeen Jeon, and Hiromichi Ohta, “Thermal conductivity tensor of NbO₂“, *International Journal of Heat and Mass Transfer* **137**, 263 (2019).

4. Hai Jun Cho, **Takaki Onozato**, Mian Wei, Anup Sanchela, and Hiromichi Ohta, “Effects of vacuum annealing on the electron mobility of epitaxial La-doped BaSnO₃ films”, *APL Mater.* **7**, 022507 (2019).

5. A.V. Sanchela, **T. Onozato**, B. Feng, Y. Ikuhara, and H. Ohta, “Thermopower modulation clarification of the intrinsic effective mass in a transparent oxide semiconductor, BaSnO₃“, *Phys. Rev. Materials* **1**, 034603 (2017).

6. **T. Onozato**, T. Katase, A. Yamamoto, S. Katayama, K. Matsushima, N. Itagaki, H. Yoshida, and H. Ohta, “Optoelectronic properties of valence-state-controlled amorphous niobium oxide”, *J. Phys. Condens. Mater.* **28**, 255001 (2016).

Book Chapter

1. 太田裕道, 小野里尚記,【第 2 編 エレクトロクロミック材料の応用】第 11 章 酸化物エレクトロクロミック材料を用いたメモリデバイスの開発「エレクトロクロミックデバイスの開発最前線」樋口昌芳 監修, シーエムシー出版

Patents

1. 太田裕道, 小野里尚記, 特願 2018-243861 「エレクトロクロミックトランジスタ、電子カーテン、情報表示記憶装置および防眩ミラー」(2018 年 12 月 27 日 出願)

Presentation lists

Presentation related to this thesis

1. Takaki Onozato, Hai Jun Cho, and Hiromichi Ohta, “A WO_3 -based electrochromic transistor on PET substrate”, The 12th International Workshop on Oxide Surfaces: IWOX-XII, Lake Placid, NY, USA, January 5-10, 2020 (Poster)
2. Takaki Onozato, Hai Jun Cho, and Hiromichi Ohta, “A flexible electrochromic transistor under mechanical fatigue”, The 3rd Workshop on Functional Materials Science, Sapporo, Japan, December 18-20, 2019. (Poster)
3. Takaki Onozato, Hai Jun Cho, Hiromichi Ohta, “Fabrication of electrochromic transistor on flexible substrate”, Materials Research Meeting 2019, Yokohama, Japan, December 10-14, 2019.
4. Takaki Onozato, Hai Jun Cho, and Hiromichi Ohta, “Flexible electrochromic transistor”, The 9th Asia-Pacific Workshop on Widegap Semiconductors (APWS2019), Okinawa, Japan, November 10-15, 2019.
5. 小野里尚記, Hai Jun Cho, 太田裕道, “ WO_3 固体エレクトロクロミックフレキシブルトランジスタの高速動作”, 2019 年 第 80 回応用物理学会秋季学術講演会, 北海道大学 札幌キャンパス, 北海道札幌市, 2019 年 9 月 18 日-21 日 (講演奨励賞受賞講演, Invited)

Presentation Lists

6. 小野里尚記, 根津有希央, Hai Jun Cho, 太田裕道, “WO₃ 固体エレクトロクロミックトランジスタの高速動作”, 2019 年 第 66 回 応用物理学会春季学術講演会, 東京工業大学 大岡山キャンパス(東京都目黒区), 2019 年 3 月 9 日-12 日
7. 小野里尚記, 片瀬貴義, 廣野未沙子, 水野 拓, 太田裕道, “3 端子 TFT 構造アモルファス WO₃ エレクトロクロミック素子の開発と動作検証”, 第 52 回応用物理学会北海道支部/第 13 回日本光学会北海道支部合同学術講演会, 北見工業大学, 北見, 2017 年 1 月 7 日-8 日
8. T. Onozato, T. Katase, M. Hirono, T. Mizuno, and H. Ohta, “Amorphous WO₃ electrochromic device with thin-film transistor electrode geometry”, The 17th RIES-Hokudai International Symposium 柔 [Ju], Chateraise Gateaux Kingdom Sapporo, Sapporo, Japan, December 13-14. 2016 (Poster)
9. 小野里尚記, 片瀬貴義, 廣野未沙子, 水野 拓, 太田裕道, “色調-導電性を同時変調可能な酸化物エレクトロクロミック素子の開発”, 日本セラミックス協会東北北海道支部研究発表会, 北海道大学 フロンティア応用科学研究棟, 札幌, 2016 年 10 月 27 日-28 日
10. 小野里尚記, 片瀬貴義, 廣野未沙子, 水野 拓, 太田裕道, “薄膜トランジスタ電極配置を有するエレクトロクロミックデバイスの室温作製”, 薄膜材料デバイス研究会, 龍谷大学 響都ホール校友会館, 京都, 2016 年 10 月 21 日-22 日(Poster)

11. 小野里尚記, 片瀬貴義, 太田裕道, “薄膜トランジスタ構造を有するアモルファス酸化物エレクトロクロミック素子”, 第 63 回 応用物理学会春季学術講演会, 東工大 大岡山キャンパス, 東京, 2016 年 3 月 19 日-22 日

Presentation lists related to other papers

1. T. Onozato, H.J. Cho, Y-M. Chang, Y-M. Sheu, B. Feng, Y. Ikuhara, H. Ohta, “Thermal conductivity anisotropy of layered complex oxide”, The 19th RIES-HOKUDAI International Symposium 組[So], Jozankei View Hotel, Sapporo, December 11-12, 2018.

(Poster)

2. T. Onozato, H.J. Cho, Y-M. Chang, Y-M. Sheu, B. Feng, Y. Ikuhara, and H. Ohta, “Anisotropic thermal conduction behavior of a complicated layered structure oxide”, The 2nd Workshop on Functional Materials Science, Busan, South Korea, October 22-23, 2018.

3. 小野里尚記, Cho Hai Jun, Yi-Ming Chang, Yu-Miin Sheu, フウ ビン, 幾原雄一, 太田裕道, “TDTR 法による層状酸化物薄膜の熱伝導率の結晶方位依存性計測”, 2018 年 第 79 回 応用物理学会秋季学術講演会, 名古屋国際会議場(名古屋・愛知), 2018 年 9 月 18 日-21 日

4. Takaki Onozato, Yi-Ming Chang, Yu-Miin Sheu, and Hiromichi Ohta, “Absence of thermal conductivity anisotropy in $\text{Ca}_3\text{Co}_4\text{O}_9$ ”, The 18th RIES-Hokudai International

Symposium 極 [Kyoku], Chateraise Gateaux Kingdom Sapporo, Sapporo, Japan,

November 30.- December 1. 2017 (Poster)

5. 小野里尚記, Yi-Ming Chang, Yu-Miin Sheu, 太田裕道, “配向制御した層状コバルト酸化物エピタキシャル薄膜の熱電特性”, 平成 29 年度日本セラミックス協会 東北北海道支部研究発表会, 東北大学片平さくらホール(宮城県仙台市), 2017 年 11 月 1 日-2 日

6. T. Onozato, T. Katase, T. Tohei, Y. Ikuhara, and H. Ohta, “Anomalous thermopower of ultrathin LaTiO₃ epitaxial layers”, International Workshop on Oxide Electronics 23, Nanjing International Conference Hotel, Nanjing, China, October 12-14. 2016 (Poster)

7. Takaki Onozato, Takayoshi Katase, Tetsuya Tohei, Yuichi Ikuhara, Hiromichi Ohta, “Anomalous thermopower of ultrathin LaTiO₃ epitaxial layers”, HOKUDAI-NCTU International Joint Symposium on Nano, Opto and Bio Sciences, Hokkaido University, Sapporo, Japan, October 4-5. 2016 (Poster)

8. 小野里尚記, 片瀬貴義, 張 雨橋, 藤平哲也, フウビン, 幾原雄一, 太田裕道, “モット絶縁体超薄膜の熱電能”, 2016 年 第 77 回応用物理学会秋季学術講演会, 朱鷺メッセ, 新潟県新潟市, 2016 年 9 月 13 日-16 日

9. 小野里尚記, 張 雨橋, 片瀬貴義, フウビン, 藤平哲也, 幾原雄一, 太田裕道, “熱電能計測と電子顕微鏡観察による、LaTiO₃/LaAlO₃ ヘテロ界面の可視化”, 新学

Presentation Lists

術領域研究「ナノ構造情報のフロンティア開拓 — 材料科学の新展開」第4回若手の会, 筑波山 江戸屋, 茨城, 2016年7月25日-26日(ポスター)

10. 小野里尚記, 片瀬貴義, 片山翔太, 太田裕道, “超平坦アモルファス NbO_x 薄膜の作製と光・電子輸送特性”, 第51回応用物理学会北海道支部学術講演会, 北海道大学 学術交流会館, 札幌, 2016年1月9日-10日

11. T. Onozato, T. Katase, S. Katayama, and H. Ohta, “Opto-electronic properties of amorphous NbO_x thin films”, THE 16th RIES-HOKUDAI INTERNATIONAL SYMPOSIUM “術” [JUTSU], Chateraise Gateaux Kingdom Sapporo, Sapporo, Japan, November 10-11. 2015 (Poster)

12. 小野里尚記, 片山翔太, 片瀬貴義, 太田裕道, “アモルファス NbO_x 薄膜の光・電子輸送特性”, 第76回 応用物理学会秋季学術講演会, 名古屋国際会議場, 名古屋, 2015年9月13日-16日

13. 小野里尚記, 片山翔太, 片瀬貴義, 太田裕道, “アモルファス NbO_x 薄膜の作製と光・電子輸送特性-新しいエレクトロクロミックトランジスタを目指して-”, 新学術領域研究「ナノ構造情報のフロンティア開拓 — 材料科学の新展開」第3回若手の会, ホテルグランテラス千歳, 北海道, 2015年7月27日-28日

Award lists

[1] 第46回(2019年春季)応用物理学会講演奨励賞 小野里尚記, 根津有希央, Hai Jun Cho, 太田裕道, “WO₃ 固体エレクトロクロミックトランジスタの高速動作”, 2019年 第66回 応用物理学会春季学術講演会, 東京工業大学 大岡山キャンパス (東京都目黒区), 2019年3月9日-12日

[2] 平成29年度日本セラミックス協会 東北北海道支部研究発表会 優秀発表賞 小野里尚記, Yi-Ming Chang, Yu-Miin Sheu, 太田裕道, “配向制御した層状コバルト酸化物エピタキシャル薄膜の熱電特性”, 東北大学片平さくらホール(宮城県仙台市), 2017年11月1日-2日

[3] Poster Award, T. Onozato, T. Katase, M. Hirono, T. Mizuno, and H. Ohta, “Amorphous WO₃ electrochromic device with thin-film transistor electrode geometry”, The 17th RIES-Hokudai International Symposium 柔 [Ju], Chateraise Gateaux Kingdom Sapporo, Sapporo, Japan, December 13-14. 2016(Poster)

[4] 平成27年度 増本賞金賞, 小野里尚記, 片山翔太, 片瀬貴義, 太田裕道, “アモルファス NbO_x 薄膜の作製と光・電子輸送特性-新しいエレクトロクロミックトランジスタを目指して-”, 新学術領域研究「ナノ構造情報のフロンティア開拓 — 材料科学の新展開」第3回若手の会, ホテルグランテラス千歳, 北海道, 2015年7月27日-28日

[5] 応用物理学会北海道支部第18回発表奨励賞, 小野里尚記, 篁 耕司, 中村基訓, 吉本健一, “Nd:YAGレーザーを用いたPLD法によるNb薄膜の作製”(2015年3月6日)